



1     **Alternating Extensional and Contractional Tectonics in the**  
2     **West Kunlun Mountains during Jurassic: Responses to the**  
3     **Neo-Tethyan Geodynamics along the Eurasian Margin**

4

5     Hong-Xiang Wu<sup>1,2</sup>, Han-Lin Chen<sup>1,2\*</sup>, Andrew V. Zuza<sup>3</sup>, Yildirim Dilek<sup>4</sup>, Du-Wei  
6     Qiu<sup>1,2</sup>, Qi-Ye Lu<sup>1,2</sup>, Feng-Qi Zhang<sup>1,2</sup>, Xiao-Gan Cheng<sup>1,2</sup>, Xiu-Bin Lin<sup>1,2</sup>

7

8     1 Key Laboratory of Geoscience Big Data and Deep Resource of Zhejiang  
9     Province, School of Earth Sciences, Zhejiang University, Hangzhou, China.

10    2 Structural Research Center of Oil & Gas Bearing Basin of Ministry of  
11    Education, Hangzhou, China.

12    3 Nevada Bureau of Mines and Geology, Nevada Geosciences, University of  
13    Nevada, Reno, NV, USA.

14    4 Department of Geology & Environmental Earth Science, Miami University,  
15    Oxford, OH, USA.

16

17    ORCID: 0000-0003-4997-8715 (Hong-Xiang Wu)

18

19    \*Corresponding author: hlchen@zju.edu.cn (Han-Lin Chen)

20

21    Address: Haina Complex Building No. 1, Zijingang Campus, Zhejiang University,  
22    866 Yuhangtang Road, Hangzhou, 310058, China.

23

24



25 **Abstract:** The Tethyan Orogenic Belt records a long-lived geological cycle  
26 involving subduction and collision along the southern margin of the Eurasian  
27 continent. The West Kunlun Mountains, located at the junction between the  
28 Tibetan and Western Asian Tethyan realm, records multiple orogenic events  
29 from the Paleozoic to the Cenozoic that shape the northwestern Tibetan  
30 Plateau. However, deciphering the complex Mesozoic contractional and  
31 extensional tectonics to interpret the broader Tethyan geodynamics remains  
32 challenging. To address the tectonic transition following the early Cimmerian  
33 (Late Triassic) collision, this study investigates the newly identified Jurassic  
34 sedimentary strata and volcanic rocks in the West Kunlun Mountains. Zircon  
35 geochronological results of basalts and sandstones reveal that this ~ 2.5-km-  
36 thick package was deposited at ca. 178 Ma, rather than the previously reported  
37 Neoproterozoic age. The alkaline basalts at the top of the formation exhibit  
38 chemical compositions similar to oceanic island basalts, consistent with the  
39 intracontinental extension environment revealed by the upward-fining  
40 sedimentary pattern. Provenance analysis, integrating conglomerate clast  
41 lithologies with detrital zircons, suggests a substantial contribution from  
42 adjacent basement sources, likely influenced by the normal faulting during initial  
43 rift stage. These findings indicate that the West Kunlun Mountains rapidly  
44 transitioned into an extensional setting after suturing with Cimmerian terranes.  
45 The regional structure, stratigraphy and magmatism suggest that this Early -  
46 Middle Jurassic basin was subsequently inverted during the Late Jurassic and  
47 earliest Cretaceous. We propose that the Mesozoic deformational history in the  
48 West Kunlun Mountains was related to the northward subduction of the Neo-  
49 Tethys Ocean, as it transitioned from southward retreat to northward flat-slab



50 advancement. Comparing with the entire strike-length of the Eurasian Tethyan  
51 orogen, we find that the subduction mode varied from the west to the east,  
52 reflecting the broad geodynamic changes to, or initial conditions of, the Neo-  
53 Tethyan system.

54

55 **Keywords:** Tethyan Orogenic Belt; West Kunlun Mountains; Jurassic volcanics;  
56 Basin evolution; Subduction retreating and advancing.

57



## 58 **1 Introduction**

59       The Tethyan Orogenic Belt, a trans-Eurasian mountain system spanning  
60 an east-west strike-length of over 15,000 km, is characterized by a series of  
61 mountain chains and orogenic plateaus along its latitudinal extent (Fig. 1a;  
62 Şengör, 1987; Metcalfe, 2013; Wu et al., 2020). The evolution of the Tethyan  
63 Orogenic Belt involved multiple phases of ocean basin opening and closing (i.e.,  
64 the Proto-, Paleo-, and Neo-Tethys oceans) throughout the Phanerozoic era,  
65 which resulted in the development of multiple orogenic belts across the  
66 Eurasian continent (Stampfli, 2000; Wan et al., 2019; Metcalfe, 2021). The  
67 complex history of accretionary and collisional orogenesis in the Tethyan realm  
68 is intricately linked to the breakup and formation of the two mega-landmasses,  
69 Gondwana and Laurasia (Şengör et al, 1988; Stampfli and Borel, 2002; Zuza  
70 and Yin, 2017; Li et al., 2018; Wang et al., 2018). Documenting the mode and  
71 nature of the accretionary and collisional events in the Mesozoic history of the  
72 Tethyan orogenic system is, therefore, important for understanding the  
73 continental dynamics of Eurasia.

74       The Mesozoic Tethyan Orogenic Belt involved a protracted phase of  
75 orogenesis, rifting, and basin evolution, associated with the convergence  
76 between the southern Asian margin and Cimmerian terranes derived from  
77 Gondwana (e.g., Kazmin, 1991; Stampfli and Borel, 2002; Angiolini et al., 2013;  
78 Robinson, 2015). The tectonic evolution of the Tethyan realm during the  
79 Mesozoic exhibits significant variations from the west to the east (Şengör, 1984;  
80 Zhu et al., 2022). In the Western Asian section of the Tethyan Orogenic Belt,  
81 geochronological and geochemical data from diverse magmatic rocks  
82 assemblages suggest a propagating continental rift system in the southern



83 margin of the Iran Block during the Early Jurassic to Early Cretaceous (Hunziker  
84 et al., 2015; Lechmann et al., 2018; Azizi and Stern, 2019). This process is  
85 envisioned to have been associated with subduction geodynamics involving  
86 multiple intraoceanic subduction zones, slab tearing, and alternating slab  
87 rollback and advance within Neo-Tethys (Zhang et al., 2018; Jafari et al., 2023).  
88 Conversely, in the Eastern Asian section of the Tethyan Orogenic Belt (i.e.  
89 Tibetan sector), an Andean-type orogeny along the southern margin of Eurasia  
90 from the Early Jurassic to the Early Cretaceous has been proposed to explain  
91 deformation and sedimentation patterns in the southern Tibetan Plateau (Kapp  
92 et al., 2007; Zhang et al., 2012; Xie and Dilek, 2023). This process was  
93 punctuated by Toarcian-Aalenian back-arc rifting event resulting from retreat of  
94 the subducting Neo-Tethyan seafloor (Hou et al., 2015; Wei et al., 2017).

95 The West Kunlun Mountains, stretching from the northern Pamir to  
96 northwestern Tibetan Plateau, occupy a critical position at the junction between  
97 the western and eastern Tethyan Orogenic Belts (Fig. 1b; Şengör, 1984; Wu et  
98 al., 2016). The Kunlun Mountains involved the closure of the Paleo-Tethyan  
99 Ocean in the Triassic-Jurassic, followed by Cenozoic deformation and uplift  
100 during the Himalayan orogeny (Mattern and Schneider, 2000; Cao et al., 2015;  
101 Li et al., 2019; Xiao et al., 2002). Hence, the Mesozoic geology of the West  
102 Kunlun Mountains documents the plate tectonic history of the junction region  
103 within the Tethyan realm, providing pivotal insights into the formation of this  
104 extensive orogenic system. In particular, the Cimmerian Orogeny in the West  
105 Kunlun region critically represents the collision between the Gondwana- derived  
106 continental fragments and the southern Eurasian margin in the latest Triassic  
107 to late Jurassic (e.g., Şengör, 1979), but the timing and duration of this orogen



108 remains equivocal. Existing interpretations of the Jurassic palaeogeography  
109 and evolution vary, ranging from syn-orogenic (Cao et al., 2015), post-orogenic  
110 (Wu et al., 2021), to transtensional (Sobel, 1999), because of the scarcity of the  
111 relevant geological record from this period. Significant challenges also persist  
112 in understanding the Mesozoic evolution of the Pamir terranes (Angiolini et al.,  
113 2013), including the timing of suturing and exact kinematics of related  
114 deformation (Robinson, 2015). The Cenozoic contractional deformation  
115 episodes, due the northward subduction of the Neo-Tethyan Ocean and the  
116 collision of India with Eurasia, further complicates our understanding in this  
117 remote region (Burtman and Molnar, 1993; Cowgill, 2010). The limited  
118 knowledge of the Jurassic and Cretaceous evolution of the Pamir interior has  
119 been preliminarily deduced from the timing and nature of regional magmatic  
120 activities (Chapman et al., 2018) that are challenged by the information derived  
121 from the surrounding, fragmented sedimentary basins (Leith, 1985; Wu et al.,  
122 2021).

123 To better understand the regional evolution and tectono-magmatic  
124 processes in the West Kunlun Mountains, we have undertaken a systematic  
125 geochronological and geochemical study and detailed analyses of sedimentary  
126 provenance of volcanoclastic rock suites in a Jurassic basin. By integrating  
127 these new results with existing data from the adjacent region, this study  
128 provides further constraints on the Mesozoic tectonic history of the central  
129 junction of the Tethyan Orogenic Belt, probing the preceding processes that  
130 cause the formation of the broad plateau in central Asia.

131



132 **2 Geological framework and sampling**

133 **2.1 Tethyan history**

134 The Tethyan Orogenic Belt is a vast, east-west-extending mountain system  
135 that separates the main Eurasian cratons and stable platforms in the north from  
136 Gondwana - derived continental terranes in the south (e.g., Şengör et al, 1988;  
137 Stampfli et al., 1991). The development of the Tethyan Orogenic Belt involves  
138 the evolution of multiple ocean basins and their seaways, including the Proto-  
139 Tethys, Paleo-Tethys, and Neo-Tethys (Stampfli, 2000; Metcalfe, 2021). These  
140 ancient ocean basins overlapped in time but closed successively as the  
141 Gondwana - derived ribbon continents (i.e., Apulia, Pelagonia, Sakarya, Tauride,  
142 and Lhasa) accreted to the southern margin of Eurasia, creating several sub-  
143 parallel suture zones stretching from the circum-Mediterranean region,  
144 Caucasus, Iranian Plateau, and continuing eastward into the Tibetan Plateau  
145 and Southeast Asia (Fig. 1a; Dilek and Moores, 1990; Wu et al., 2020; Metcalfe,  
146 2021).

147 The Cenozoic indentation of the Pamirs fundamentally affected the  
148 deformation pattern of the Tethyan Orogenic Belt and geographically divided  
149 the belt into western and eastern sectors (Tapponnier et al., 1981). The history  
150 of the Proto-Tethys was linked to the breakup of the Rodinia supercontinent  
151 (Zhao et al., 2018). The western segment of the Proto-Tethys has been defined  
152 as a Cambrian-Silurian ocean existing between Baltica and Gondwana,  
153 whereas the eastern Proto-Tethys appears to have been closed earlier in the  
154 Early Silurian, as a series of Asian blocks collided onto the northern margin of  
155 Gondwana (e.g., Stampfli and Borel, 2002). The opening of the Paleo- and Neo-  
156 Tethyan ocean basins was related to slab pull forces that caused the



157 detachment of the Hun (including the Tarim, North and South China) and  
158 Cimmerian terrane ribbons from the northern margin of Gondwanaland,  
159 respectively (Stampfli and Borel, 2002; Ruban et al., 2007). These terranes  
160 were successively transferred northward to the Eurasian continent, causing the  
161 closure of these internal seaways during the Cimmerian and Himalayan  
162 orogenies at the end of the Triassic and the beginning of the Cenozoic,  
163 respectively (Dilek and Furnes, 2019; Wan et al., 2019).

164 The final demise of the Paleo-Tethyan Ocean and the initiation of  
165 subduction in the Neo-Tethyan Ocean occurred simultaneously in the Triassic -  
166 earliest Jurassic, which is of vital importance for comprehension of the cyclical  
167 Tethyan evolution (Wan et al., 2019). The West Kunlun Mountains, situated to  
168 the north of the Pamir syntaxis, forms the western extent of the Tibetan Plateau  
169 (Fig. 1b-c). They constitute an important spatial link between the western and  
170 eastern domains of the Tethyan Orogenic Belt. The formation of the West and  
171 East Kunlun Mountains, involved accretionary and collisional orogenesis  
172 during the closure of the Proto-Tethys and Paleo-Tethys oceans (Mattern and  
173 Schneider, 2000; Xiao et al., 2005; Dong et al., 2018). The East Kunlun  
174 Mountains are deflected to the north relative to the West Kunlun Mountains by  
175 the dextral Altyn-Tagh strike-slip fault (Fig. 1b). During the Early Paleozoic, the  
176 closure of the Proto-Tethys Ocean led to the collision of the Tarim Craton (North  
177 Kunlun) and the South Kunlun terrane along the Kudi suture zone (Fig. 1c;  
178 Zhang et al., 2019a). After splitting from eastern Gondwana in the Devonian -  
179 Carboniferous, the Tianshuihai - Qiangtang blocks travelled northward towards  
180 the Tarim Craton because of the subduction of the Paleo-Tethyan Ocean floor.  
181 These blocks ultimately collided with the Tarim Craton at the latest Triassic,





182 forming the Mazar - Kangxiwa suture zone (Fig. 1c; Xiao et al., 2005; Metcalfe,  
183 2021). The Pamir terranes (including the Central Pamir, South Pamir, and  
184 Karakoram), commonly regarded as the western counterpart of the Qiangtang  
185 block, rifted from Gondwana much later, during the Permian (Robinson, 2015;  
186 Angiolini et al., 2015). The major Cimmerian orogenic unconformity between  
187 the Lower Jurassic and the deformed Upper Triassic strata is generally  
188 considered to mark the timing of the integration of these Pamir terranes onto  
189 the Eurasian margin (Angiolini et al., 2013; Li et al., 2022b).

190 The mid-Mesozoic tectonic evolution of the West Kunlun Mountains and  
191 Pamir is somewhat enigmatic, as the first-order geodynamic mechanisms for  
192 widespread observed deformation remain unclear. The interpretation of  
193 Jurassic molasse deposits has led to differing understandings on the tectonic  
194 setting in the region, such as syn-orogeny or post-collisional rifting (Gaetani et  
195 al., 1993; Wu et al., 2021). Several major exhumation events, including the Late  
196 Triassic and Early Jurassic, Middle-Late Jurassic, Early Cretaceous, and Late  
197 Cretaceous, are documented by low-temperature thermochronology in the  
198 mountain ranges and surrounding basins (Sobel, 2013; Cao et al., 2015; Li et  
199 al., 2019, 2023). Mid-Cretaceous granitoid plutons are widespread in the South  
200 Pamir and Karakoram. A polymetamorphic Jurassic and Cretaceous history of  
201 the mountains is also displayed by monazite ages (Faisal et al., 2014). The  
202 basement cooling as well as magmatic, and metamorphic events have  
203 previously been interpreted as associated with far-field stress effects of  
204 collisional events (Yang et al., 2017) or a high-flux event during an Andean-type  
205 subduction of the Neo-Tethyan Ocean (Chapman et al., 2018). These Mesozoic  
206 structures within the orogenic belts were intensely reworked by the Cenozoic



207 deformation during the Himalayan orogeny (Burtman and Molnar, 1993).

208

## 209 **2.2 Regional geology and sampling strategy**

210 This study focused on the central and southern parts of the northwest-  
211 trending Jurassic basin within the West Kunlun Mountains (Fig. 1c). The  
212 Kyzyltau region, situated in the central part of this Jurassic basin, preserves the  
213 thickest Early-Middle Jurassic strata. It mainly comprises the Lower Jurassic  
214 Shalitashi and Kangsu formations, and the Middle Jurassic Yangye and Taerga  
215 formations (Fig. 2a). The Shalitashi Formation comprises a massive, thick  
216 conglomerate that overlies the deformed Carboniferous and Permian shallow  
217 marine clastic rocks and limestones along an angular unconformity (Fig. 3a).  
218 The poorly sorted textures and lateral thickness variations in the conglomerate  
219 indicate that its clastic material originated from alluvial fans (Sobel, 1999; Fig.  
220 3b). The Kangsu and Yangye formations form the main part of the Jurassic  
221 strata (Fig. 2a), with total stratigraphic thickness exceeding 1800 meters. The  
222 Kangsu Formation mainly comprises stacked greywackes interbedded with  
223 coal layers. The Yangye Formation consists mainly of interbedded sandstones  
224 and shales exhibiting typical Bouma sequences, indicative of turbidite deposits  
225 in a deepwater environment (Wu et al., 2021). The Middle Jurassic Taerga  
226 Formation is only exposed in the northeastern side of the region and consists  
227 of thinly-bedded shales and siltstones. The Lower to Middle Jurassic  
228 stratigraphy forms an upward-fining sequence, indicating the expanding and  
229 deepening of the basin over time. Structurally, the Jurassic strata exhibit strong  
230 deformation, forming a northwest-trending synclinorium (Fig. 2a). The Cenozoic  
231 contraction in the region extensively deformed the coal-bearing strata, resulting



232 in the formation of multi-scale folds and thrusts (Fig. 3c and 3d). Regionally, the  
233 Early-Middle Jurassic strata are unconformably overlain by the Late Jurassic  
234 Kuzigongsu Formation and the Cretaceous Kezilesu Group, which are  
235 characterized by oxidation-colored, massive conglomerate and sandstones  
236 (Fig. 3e). This event was generally interpreted to have been linked to the Middle  
237 - Late Jurassic, large-scale contraction and aridification across central Asia  
238 (Hendrix et al., 1992; Yang et al., 2017).

239 Documentation and study of the Mesozoic stratigraphy in the southernmost  
240 part of the Jurassic basin have been relatively insufficient. In the Kandilik region,  
241 geological mapping identified a coal-bearing formation, known as the Lower -  
242 Middle Jurassic Yarkant Formation, and a massive conglomerate classified as  
243 the Upper Jurassic Kuzigongsu Formation (Fig. 2b). These Jurassic strata were  
244 strongly deformed and laterally bounded by a mylonitic shear zone to the west  
245 and thrust faults to the east. A stratigraphic unit of gray-black slate interbedded  
246 with fine sandstones and siltstones is exposed to the east of the Yarkant  
247 Formation, with a thickness exceeding 3500 meters (Ma et al., 1991). Abundant  
248 mafic dykes intruded into the lower part of the strata (Fig. 3f), causing local  
249 contact metamorphism. A suite of volcanic strata composed of several basalt  
250 layers are juxtaposed with the thick clastic package along a steeply-dipping  
251 fault. Several eruptive episodes are identified within this unit based on  
252 alternating volcanic horizons, including volcanic breccia (Fig. 3g), amygdaloidal  
253 basalts, and massive basalts (Fig. 3h). These volcanic rocks belong to the part  
254 of upper member deposited above the thick clastic strata (Ma et al., 1991). Due  
255 to the lack of reliable constraints from chronological results, this stratigraphic  
256 unit has long been thought as Precambrian in age (Ma et al., 1991). Structurally,



257 the strata were intensely deformed by regional Kashgar-Yecheng transfer faults  
258 (Fig. 2) and bedding dips steeply to the northeast (Fig. 3i).

259 In the Kandilik region, one basalt sample (AYBL09) was collected near the  
260 thrust fault for geochronological dating (Fig. 2b). Six fresh, undeformed basalt  
261 samples were also obtained away from faults for geochemical analysis. These  
262 basaltic rock samples consist primarily of plagioclase with a fine columnar  
263 texture and anhedral Ti-Fe oxides (Fig. 3j). Plagioclase is locally altered into  
264 chlorite. Additionally, one quartz-lithic sandstone sample (AYBL13) was  
265 collected for detrital zircon age analysis. This sample exhibits poor sorting and  
266 is composed mainly of quartz (~ 30%) with angular shapes, feldspar (<10%),  
267 and lithic fragments (> 60%) (Fig. 3k). For regional comparison, two sandstone  
268 samples were collected from the Kangsu (KZLT1601) and Yangye formations  
269 (KZLT1602) in the Kyzyltau region (Fig. 2a). These sandstones show similar  
270 textures and compositions to the clastic sample from the Kandilik region (Fig.  
271 3l).

272

### 273 **3 Methodology**

274 One basalt sample (AYBL09) was collected from the Kandilik region for  
275 zircon U - Pb geochronology and in-situ trace element analysis. Zircon  
276 separation and cathodoluminescence (CL) imaging were done at Yuheng Rock  
277 & Mineral Technology Service Co., LTD., Langfang, China. Zircons were  
278 analyzed for U - Pb geochronology using an Agilent 8900 ICP-QQQ equipped  
279 with an ESI New Wave NWR 193UC (Two Vol2) laser ablation system at Beijing  
280 Quick-Thermo Science & Technology Co., Ltd, China. Concordia plots were  
281 constructed using IsoplotR (Vermeesch, 2018).



282 To analyze the petrogenesis and tectonic setting of magmatism, six fresh  
283 basalt rocks were collected from the same section for determining their major  
284 and trace element chemistry. Samples were first crushed, and powdered in an  
285 agate mill. Elemental analyses were conducted at Wuhan SampleSolution  
286 Analytical Technology Co., Ltd. Major-element analyses were performed by X-  
287 ray fluorescence spectrometry (ZSXPrimusII), with analytical uncertainties  
288 generally better than 1%. Trace-element contents were determined using an  
289 Agilent 7700e ICP-MS.

290 To compare the detrital age patterns and sedimentary provenance, we  
291 have conducted zircon U-Pb dating on two sandstones (KZLT1601 and KZLT1602)  
292 exposed in the Kyzyltau section, and one sandstone (AYBL13) exposed in the  
293 Kandilik section (Fig. 2B). Zircons from samples KZLT1601 and KZLT1602 were  
294 analyzed for U - Pb geochronology using a Thermofisher iCAP RQ ICP-MS  
295 equipped with a Cetea Analyte HE laser ablation system at School of Earth  
296 Sciences, Zhejiang University. Zircons from sample AYBL13 were analyzed for  
297 U - Pb geochronology using an Agilent 8900 ICP-QQQ equipped with an ESI  
298 New Wave NWR 193UC (Two Vol2) laser ablation system at Beijing Quick-  
299 Thermo Science & Technology Co., Ltd. The Common Pb was corrected with  
300 the method proposed by (Andersen, 2002). Concordia plots and Kernel Density  
301 Estimate (KDE) plots were constructed using IsoplotR (Vermeesch, 2018) and  
302 Density Plotter 8.5 (Vermeesch, 2012), respectively.

303 The details of the analytical procedures and the information of the  
304 analytical methodologies, as explained above, are presented in Table S1.

305 The data from the conglomerate in the Shalitashi Formation were collected  
306 at eight different sections. Analysis of conglomerate clasts was conducted



307 within a designated 1 square meter area. Our focus was on documenting the  
308 lithological compositions of the clasts, with at least one hundred gravels  
309 randomly counted at each site.

310

## 311 **4 Analytical Results**

### 312 **4.1 Morphology and geochronology of zircons from basalt samples**

313 The results of zircon U-Pb dating of the basalt sample are presented in  
314 Table S2. Approximately one hundred and seventy zircon grains have been  
315 successfully separated from the basalt sample. Zircon crystals are mostly  
316 transparent and colorless, displaying varying lengths ranging between 50-200  
317  $\mu\text{m}$  with elongation ratios of 1:1-5:1 (Fig. 4). Upon examination of their  
318 cathodoluminescence (CL) images, we have sub-categorized these zircons into  
319 two groups based on the presence of oscillatory zoning. The grains showing  
320 well-defined growth zoning are generally sub-euhedral in shape (no.3 in Fig. 4),  
321 which imply their magmatic origin (Fig. 4; Hoskin and Schaltegger, 2003).  
322 Another type of zircon displays inconspicuous zoning texture or yields only  
323 faintly visible zoning patterns (no.15 in Fig. 4). Morphological analysis of these  
324 zircons reveals a range from needle-shaped and elongated crystals (no.13 in  
325 Fig. 4) to stubby and equant forms (no.12 in Fig. 4). A common feature of these  
326 varying grains is their subrounded external appearance. This may result from  
327 moderate resorption either during the evolution of the magma chamber when  
328 the magma is oversaturated with respect to zircon or a certain degree of  
329 metamorphism (Corfu et al., 2003). In addition to their "polished" shape, these  
330 zircons commonly display nebulous or patchy-zoned centers, without distinct  
331 core-rim structures (no.11-13 in Fig. 4).



332 We have conducted a total of thirty-six spot analyses on various types of  
333 zircons, resulting in thirty-three analyses with a > 90% concordance (Fig. 5a).  
334 The Th/U ratios of these zircons range from 0.04 to 1.52 (Fig. 5d). We cannot  
335 assert that all of them are primary crystals without modification simply based  
336 on the evaluation of Th/U ratios. However, all of these results yielded  
337 concordant ages spanning a broad range from the Early Neoproterozoic to the  
338 Jurassic. Twenty youngest zircons with the concordant ages define a weighted  
339 mean  $^{206}\text{Pb}/^{238}\text{U}$  age of  $178 \pm 2$  Ma (MSWD = 0.99) (Fig. 5b). We interpret this  
340 Toarcian age as the crystallization age of the zircons in this rock sample. The  
341 remaining older zircons yield primarily middle Paleozoic and Neoproterozoic  
342 ages, which we interpret as inherited from the country rock.

343

#### 344 **4.2 Detrital zircon U–Pb ages from Jurassic sandstone**

345 The zircon U-Pb geochronological dataset for the detrital zircons is  
346 presented in Table S2. A total of 101 spot analyses were conducted on zircon  
347 grains from sample AYBL13. After filtering grains with greater than 10% age  
348 discordance, 98 of them met the criteria for inclusion in the Kernel Density  
349 Estimate (KDE) visualization (Fig. 6a). The analyzed results reveal that the  
350 Th/U ratios of most effective zircons range between 0.12 and 2.61, with only  
351 four zircons yielding extremely low values below 0.1 (Fig. 5d). The results  
352 suggest that most detrital zircons from sample AYBL13 are of igneous origin  
353 (Belousova et al., 2002). The youngest zircon grain from this sandstone yielded  
354 an apparent  $^{206}\text{Pb}/^{238}\text{U}$  age of  $429 \pm 5$  Ma, whereas the oldest grain has  
355 revealed an apparent  $^{206}\text{Pb}/^{207}\text{Pb}$  age of  $3080 \pm 22$  Ma. The KDE plot reveals  
356 four main age populations with peaks at approximately 446 Ma, 820-955 Ma,



357 1553 Ma, and 2484 Ma (Fig. 6b).

358 For analyzing regional detrital provenance, two Jurassic samples from  
359 Kyzyltau were analyzed for age comparison. The Early Jurassic sample  
360 KZLT1601 underwent one hundred spot analyses on randomly selected zircon  
361 grains. These measured grains exhibit Th/U ratios ranging from 0.09 to 1.49  
362 (Fig. 5d), consistent with an igneous origin. Eighty-nine zircon ages were  
363 plotted on or near the concordant curve (Fig. 6c), providing zircon ages ranging  
364 from  $369 \pm 6$  Ma to  $3314 \pm 15$  Ma. The detrital age spectrum was obtained using  
365 the KDE method and revealed similar peaks at approximately 444 Ma, 807 Ma,  
366 1823 Ma, and 2566 Ma (Fig. 6d).

367 Similarly, one hundred zircon grains from the Middle Jurassic sample  
368 KZLT1602 exhibit characteristics indicative of a magmatic origin, with high Th/U  
369 ratios ranging between 0.11 and 2.63 (Fig. 5d). Ninety - eight concordant results  
370 display consistent age population with the sample KZLT1601, ranging from  $345$   
371  $\pm 4$  Ma to  $3029 \pm 15$  Ma (Fig. 6e). These age populations on the KDE plot also  
372 display four main peaks at approximately 435 Ma, 782-988 Ma, 1829 Ma, and  
373 2480 Ma (Fig. 6f).

374

#### 375 **4.3 Analysis of Jurassic conglomerate clast lithologies**

376 The field provenance analysis of the Lower Jurassic conglomerate  
377 (Shalitashi Formation) reveals significant variations in composition across  
378 different sections. In the Kangsu and Wulagen sections, located in the  
379 northernmost region of the West Kunlun Range, clasts are composed  
380 predominantly of green sandstones (80-51%) and low-grade metamorphic  
381 rocks like schist (0-46%), with minor occurrences of light-colored siliceous rock





382 (14-3%) and granitoid (6-0%). In the northwestern sector of the Pamir, a  
383 variegated sandstone (22-46%) and a recycled siliceous rock (29-46%)  
384 predominantly constitute major clasts in the Oyttag and Gaizi sections,  
385 respectively. Additionally, minor limestone (11-2%) and diverse igneous rocks  
386 (38-6%), including granitoids, rhyolite, and basalts occur characteristically in  
387 the same stratigraphic horizon. In the Kyzyltau section, the clasts of the  
388 Jurassic conglomerate are dominated by green-colored sandstone (28%) and  
389 granites (50%) with subordinate schist (13%) and siliceous rock (9%). To the  
390 south of Kyzyltau, the Tamu and Qimugen sections present a provenance  
391 source dominated by sedimentary rocks. Clasts of limestone and green  
392 sandstone account for 85% and 61% in the neighboring sections, respectively.  
393 The proportion of reddish sandstone in the Qimugen section (33%) surpasses  
394 that in the Tamu section (15%). The Kusilafu section, located to the north of the  
395 Kandilik region, exhibits similar clast lithologies in the conglomerate to the  
396 Qimugen section, with a predominance of green sandstone (34%) and recycled  
397 siliceous rock (45%), along with minor occurrences of reddish sandstone (16%).  
398 Detailed clast lithologies and counting results are presented in the Table S4.

399

#### 400 **4.4 Whole-rock major and trace elements of basalts**

401 The chemical compositions of the basalt samples from the Kandilik section  
402 are provided in Table S5. Except for one sample (AYBL11D), the majority of our  
403 samples displays similar geochemical compositions, characterized by low SiO<sub>2</sub>  
404 (45.7-51.0 wt.%) and MgO (4.78-7.18 wt.%) contents, and Mg#s ranging  
405 between 45 and 52. These samples possess high TiO<sub>2</sub> (2.42-3.34 wt.%) and  
406 total alkali (Na<sub>2</sub>O+ K<sub>2</sub>O = 5.17-6.35 wt.%) contents, exhibit moderate Al<sub>2</sub>O<sub>3</sub>



407 contents ranging from 11.1 to 14.4 wt.% and total Fe<sub>2</sub>O<sub>3</sub> ranging from 12.6 to  
408 13.7 wt.%. In comparison, the sample AYBL11D displays relatively high  
409 contents of SiO<sub>2</sub> (55.5 wt.%) and TiO<sub>2</sub> (4.76 wt.%) with a low total alkali content  
410 (4.80 wt.%). All basalt samples fall within the alkaline series field as depicted in  
411 the total alkali-silica diagram (Fig. 7a). However, it is worth noting that all  
412 analyzed samples exhibit varying Lost-on-Ignition (LOI = 1.51-9.81 wt.%)  
413 values, attributed to weathering and alteration effects, with the presence of  
414 chlorite and calcite (Fig. 3j). Hence, it is crucial to assess the alteration effects  
415 on the chemical compositions of the analyzed samples. The high-field-strength  
416 elements (HFSE, such as Nb, Ta, Ti, and Hf) and rare earth elements (REE)  
417 are typically immobile during alteration. This is supported by the consistent  
418 elemental variations against the most immobile element Zr, as shown in the Fig.  
419 S1. Additionally, Cr and Ni in these samples (except AYBL11D) also  
420 demonstrate strong correlations with Zr, suggesting that these elements were  
421 essentially immobile during alteration. Based on the Nb/Y vs. Zr/TiO<sub>2</sub> diagram  
422 proposed by Winchester and Floyd (1977), all samples plot in the alkaline series  
423 (Fig. 7b). Therefore, we posit that these rocks are best classified as alkaline  
424 basalt.

425 All analyzed samples display consistent chondrite-normalized rare earth  
426 element patterns (Fig. 7c), characterized by an enrichment of LREE relative to  
427 HREE, with (La/Yb)<sub>N</sub> ratios ranging from 6.24 to 7.96. Moreover, their REE  
428 patterns exhibit slight negative Eu anomalies ( $\delta\text{Eu} = 0.7\text{-}1.0$ ). The primitive  
429 mantle-normalized multi-element diagram illustrates that the analyzed samples  
430 are characterized by the enrichment of highly incompatible trace elements  
431 relative to low incompatible elements (Fig. 7d). The samples present significant



432 depletion of Sr and slight enrichment in Zr and Hf. No negative Zr-Hf-Ti  
433 anomalies are observed in any of the analyzed basalts.

434

### 435 **5 Identification and age constraints for the Lower Jurassic strata**

436 Identified Jurassic strata are largely exposed in the eastern edge of the  
437 West Kunlun Mountains and on the southern side along the Talas-Fergana  
438 Fault (Fig. 1c). The Jurassic sequences are comprised of coal-bearing  
439 siliciclastic rocks with variable thicknesses (Wu et al., 2021). Jurassic volcanic  
440 strata have not been previously identified in the West Kunlun Mountains,  
441 although a Jurassic tuffaceous succession and Upper Triassic - Lower Jurassic  
442 volcanic rocks crop out in the Hindu Kush along the western edge of the Pamir  
443 (Brookfield and Hashmat, 2001). Our study has focused on a package of thick  
444 clastic rocks intercalated with basaltic lavas, are exposed in the southernmost  
445 part of the Jurassic Kyzyltau syncline (Fig. 2). This stratigraphic package was  
446 previously considered to be of Mesoproterozoic or Neoproterozoic age due to  
447 the lack of fossil records and the presence of low-degree metamorphism (Ma  
448 et al., 1991). Lithologically, the monotonous clastic member is composed  
449 primarily of gray-black slate and fine - grained sandstone to siltstone, rich in  
450 iron and carbonaceous components (Ma et al., 1991). The overlying basalts  
451 vary significantly in their thickness and lithological makeup, composed primarily  
452 of basaltic volcanic breccia, amygdaloidal, and massive layers (Fig.3g and 3h).

453 Our new results of zircon U-Pb dating of basalts and sandstones suggest  
454 that this rock assemblage is not Precambrian in age, given the widespread  
455 appearance of Phanerozoic ages. We suggest that the weighted mean  
456  $^{206}\text{Pb}/^{238}\text{U}$  age (~178 Ma) of the youngest group of zircons separated from the



457 basalt sample could define the eruptive age of this magmatic episode based on  
458 the following lines of evidence. First, these zircons exhibit similar morphological  
459 and CL imaging characteristics (Fig. 4), with the majority of the analyzed grains  
460 displaying Th/U ratios indicating their igneous origin (Fig. 5d). Secondly, the  
461 results of our in-situ trace elemental composition of the zircons (Table S3)  
462 indicate that the chondrite-normalized rare earth elements consistently exhibit  
463 left-sloping pattern with positive anomalies in Ce and Sm, and negative  
464 anomalies in Eu, similar to those of typical igneous zircons (Fig. 5c; Hoskin and  
465 Schaltegger, 2003). Thirdly, according to the Y vs. Yb/Sm plot proposed by  
466 Belousova et al. (2002), these Jurassic zircons are consistent with the basic or  
467 ultrabasic igneous origin (Fig. 5e). Thus, we posit that the crystallization age of  
468 the basalt is Toarcian.

469 To refine the depositional age of the clastic member of the stratigraphy, we  
470 have compared the detrital zircon results from the feldspar lithic sandstones  
471 with those from the Lower and Middle Jurassic strata, exposed in the Kyzyltau  
472 region. The sandstone collected from the Kangsu Formation displayed similar  
473 texture and composition to the rocks from the Kandilik region, both composed  
474 of immature and poorly sorted quartz and lithic fragments (Fig. 3k and 3i). The  
475 age patterns of detrital zircons display remarkably similar populations with Early  
476 Silurian (~440 Ma) and Tonian (~800-950 Ma) dominated peaks, indicating that  
477 sediments of the two investigated areas shared a common exhumed  
478 provenance. The Lower and Middle Jurassic sedimentary rocks were previously  
479 suggested to have been deposited within structural half grabens and mostly  
480 sourced from the West Kunlun Mountains (Chen et al., 2018). This  
481 interpretation is consistent with our findings. Furthermore, we infer that this



482 stratigraphic package resembles a turbidite sequence, exhibiting relatively  
483 proximal, deep-water depositional features.

484 Accordingly, we propose reassigning this thick package of clastic rocks to  
485 the Early - Middle Jurassic age. Hereon, we demonstrate the structural  
486 compatibility of this new stratigraphic scheme. The Lower - Middle Jurassic  
487 strata of the Yarkant Formation in the studied region comprise a lacustrine  
488 association rich in coal beds, and it delineated structurally by a mylonite zone  
489 to its west (Fig. 2b). The redefined sequences are rich in carbonaceous  
490 components and are closely bounded by Jurassic coal-bearing strata along  
491 several reverse faults. These two units successfully extend into the NW-SE-  
492 striking Jurassic graben, which surprisingly narrows rapidly towards the south  
493 without any obvious facies transition (Fig. 1c). The basin-ward dipping of the  
494 strata constituted the western limb of the Jurassic syncline, which has a  
495 comparable thickness that may extend into the southern area of the Kyzyltau  
496 syncline (Fig. 2).

497

## 498 **6 Discussion**

### 499 **6.1 Generation and geological setting of the Early Jurassic volcanism**

500 The basalt samples are characterized by varying  $\text{SiO}_2$  (45.7-55.5 wt.%)  
501 and low Mg# values (45-52), suggesting that they were not derived from the  
502 primary magmas, and that they likely experienced crustal assimilation and  
503 fractional crystallization (AFC) processes. Generally, mantle - derived magmas  
504 suffer various degrees of crust contamination en-route from magma chambers  
505 to the surface (Aitcheson and Forrest, 1994). The presence of inherited  
506 Paleozoic and Neoproterozoic zircons in these basalts suggests the potential



507 interactions between the ascending magmas and the country rocks (Fig. 5a).  
508 However, these basaltic rocks exhibit no negative anomalies of Nb, Ta, and Ti,  
509 which are typically depleted in the crust (Fig. 7d). They exhibit low La/Nb ratios  
510 (0.53 - 1.15) and mostly have high Nb/U ratios (37 - 45), similar to the range of  
511 oceanic lavas (La/Nb <1.2 and Nb/U >39; Krienitz et al., 2006). Additionally, all  
512 basalt samples exhibit low Th/Nb ratios (0.09-0.15), plotting along the  
513 MORB–OIB array of oceanic basalts within the Th/Yb–Nb/Yb diagram (Fig. 7e;  
514 Pearce, 2008). These signatures, with little indication of crustal components,  
515 suggest that these basalts experienced negligible contamination during their  
516 journey to the surface. They are characterized by extremely low concentrations  
517 of Ni (27.4–61.2 ppm) and Cr (25.4–108 ppm). They also exhibit slight negative  
518 anomalies of Eu and Sr on the whole-rock normalized REE patterns and spider  
519 diagram (Fig. 7c and 7d). These features could be caused by varying degrees  
520 of fractional crystallization processes involving olivine, clinopyroxene, and  
521 plagioclase.

522 The Early Jurassic episode of volcanism in the West Kunlun Mountains  
523 temporally followed the Cimmerian Orogeny. Regionally, the eruption of basalts  
524 at 178 Ma was slightly later than the peak metamorphism of high-pressure  
525 granulite facies that has been proposed to have occurred between 200 and 185  
526 Ma (Qu et al., 2021). Collisional orogeny commonly transitions from syn-  
527 collisional metamorphism to post-collisional unroofing (Dilek and Altunkaynak,  
528 2007, 2010; Zheng et al., 2019). The unroofing phase could generate  
529 geochemically varying granitoids with extrusion of mafic magma (Harris et al.,  
530 1986; Zhou et al., 2021). However, distinguishing post-collisional from syn-  
531 collisional magmatism may present challenges, because the post-collisional



532 mafic rocks could inherit whole-rock geochemical fingerprints from the  
533 preceding subducted materials (Zhao et al., 2013). Conversely, intraplate  
534 magmas are typically dominated by low-degree partial melting and silica-  
535 unsaturated alkaline magmas, which is distinct from syn- and post-collisional  
536 igneous rocks (Dilek and Altunkaynak, 2010; Xu et al., 2020).

537 The Jurassic alkali basalts exhibit enrichment of LREE and HSFES without  
538 obvious crustal signatures (e.g., Nb-Ta depletion; Fig. 7c-d), different from the  
539 syn- and post-collisional magmas in the West Kunlun Mountains (Liao et al.,  
540 2012; Chen et al., 2021). Their compositions resemble those of intraplate OIBs  
541 and could have been generated by low-degree partial melting (~5%) of a garnet  
542 lherzolite mantle source (Fig. 7e-f). All tectonic discrimination plots using  
543 immobile trace elements indicate that the Jurassic basalts formed within an  
544 intraplate setting (Fig. 8).

545 The generation of these magmas can be attributed to one of two  
546 mechanisms. The first explanation is that the North Kunlun region experienced  
547 rapid orogenic collapse after Late Triassic collisional orogeny, during which  
548 intra-plate collapse-related volcanism generate the observed basalt flows. We  
549 do not find this hypothesis plausible given the implied rapid transition from peak  
550 collisional orogeny, including ca. 185 Ma prograde metamorphism, to collapse  
551 and volcanism recorded at ca. 175 Ma (Wu et al., 2021). Many arc-continent or  
552 continent-continent collisional orogens, evolving from peak orogenic  
553 metamorphism, to orogenic collapse, to intraplate stage, collectively persist for  
554 tens of millions of years (Dewey, 2005; Weller et al., 2021).

555 Conversely, a broad plate-boundary extensional process may have  
556 impacted this orogenic belt and its hinterland region in the Early Jurassic.



557 Support for this model includes the expansive extensional rifts developed  
558 across the interior Eurasia during the Early-Middle Jurassic (e.g., Amu–Dar’ya,  
559 Afghan–Tajik and Fergana basins; Otto, 1997). The opening of the Greater  
560 Caucasus - proto-South Caspian Sea back-arc basin at the southern Eurasian  
561 margin nearly at the same time has been ascribed to a slab retreat event within  
562 the Neo-Tethys (Golonka, 2004). Back-arc transgression and MORB-like  
563 magmas have been also identified in the Tianshuihai terrane (Fig. 7; Jian et al.,  
564 2019), suggesting the slab-pull effect on the studied region in the West Kunlun  
565 Mountains. In this scenario, the Early Jurassic basalts were generated during  
566 regional extension across the region, accompanied by intra-plate volcanism.

567

## 568 **6.2 Jurassic basin formation and implications for sedimentary** 569 **provenance**

570 The closure of the Paleo-Tethyan Ocean led to collision of the Cimmerian  
571 terranes with Eurasia that caused the development of a regional unconformity  
572 across the central Asia during the Triassic to Early Jurassic (Gaetani et al., 1993;  
573 Schwab et al., 2004; Fürsich et al., 2017). This orogenic unconformity  
574 separates the imbricated Triassic flysch strata below from the overlying Middle  
575 Jurassic limestones in the Tianshuihai-Qiangtang block (Zhao et al., 2000). In  
576 the studied area, the deformed Upper Paleozoic strata are unconformably  
577 overlain by a Lower Jurassic conglomerate (Fig. 9). Analysis of the Lower  
578 Jurassic deposits suggests a regional transtension following the Cimmerian  
579 collision (Sobel, 1999). Analysis of the available seismic data identifies the  
580 Jurassic horst-graben patterns, favoring the extensional setting within basin  
581 interior (Zhao et al., 2020; Li et al., 2022a).





582           The Kyzyltau basin preserves the most comprehensive record of the  
583 formation and evolution of a post-Cimmerian rift, spanning from its initiation in  
584 the Early Jurassic to its inversion in the Late Jurassic (Wu et al., 2021). The  
585 basement of this basin varies along its lateral extent, indicating its strong  
586 tectonic reworking prior to Jurassic deposition. It comprises four subdivisions  
587 from the north to the southeast: (1) An Early Devonian metasedimentary rock  
588 terrane in the Kashgar depression (1-4 in Fig. 9), (2) The Carboniferous island-  
589 arc crust and Permian back-arc basin successions in the northwestern segment  
590 of the West Kunlun orogenic belt (5-6 in Fig. 9), (3) An Upper Carboniferous to  
591 Middle Permian platform successions in the middle segment (7-11 in Fig. 9),  
592 and (4) An Upper Permian clastic formation in the southern part (12-17 in Fig.  
593 9).

594           The massive conglomerate of the Shalitashi Formation indicates rapid  
595 infilling of the Jurassic basin during its initial opening stage in the West Kunlun  
596 orogenic belt. Analysis of conglomerate clast lithologies suggests that different  
597 sites exhibit sharp variations in their compositions, consistent with the presence  
598 of local basement rocks (Fig. 9). For example, the gravels in the Kashgar  
599 depression are mainly derived from sandstone strata, pointing to the source of  
600 the underlying Devonian (Wulagen) uplift. The gravels from the Oyttag and Gaizi  
601 sections show complex compositions, with abundant igneous and siliceous rock  
602 fragments, which might have been provided by the local arc and back-arc basin  
603 lithologies. Contrastively, gravels from the Tamu section are composed  
604 predominately of limestones, implying their origin from the underlying  
605 Carboniferous marine strata. Gravels from the Qimugen and Kusilafu sections  
606 share a similar arenaceous source region, which exists in the Devonian and



607 Permian strata in the core of the Kashgar-Yecheng syncline (Fig. 2a).

608       The Lower Jurassic strata rapidly transition from alluvial fan deposits into  
609 fluvial sedimentary environment, which is indicated by the Middle Jurassic,  
610 stacked coal-bearing sandstones of the Kangsu Formation (Fig. 9). During the  
611 Middle Jurassic, extensional faulting across the half-grabens further deepened  
612 the basin and facilitated the deposition of a turbidite sequence of the Yangye  
613 Formation (Wu et al., 2021). Provenance analysis based on detrital zircon age  
614 dating suggests that the source region for these sandstones was dominated by  
615 Late Ordovician-Early Silurian (~ 446 - 435 Ma) and Neoproterozoic (~ 980 -  
616 780 Ma) igneous rocks, with minor Neoproterozoic and  
617 Mesoproterozoic ages (Fig. 6). Early Paleozoic (~ 480 - 440 Ma) granitoids,  
618 with a peak intrusive at ~ 440 Ma (Fig. 1c; Tao et al., 2024), are exposed  
619 extensively in the South Kunlun terrane. However, the South Kunlun terrane is  
620 unlikely to be the source for these Jurassic depositions because the South  
621 Kunlun region contains extensive Triassic (~ 240 - 210 Ma) granitoids, intruded  
622 into the early Paleozoic rock units (Fig. 1c; Chen et al., 2021). Yet, Triassic  
623 detrital zircons are absent in the Lower - Middle Jurassic strata (Fig. 6).  
624 Therefore, we instead suggest that the potential source area was most likely  
625 the North Kunlun terrane, which consists mainly of Paleozoic strata and  
626 Precambrian metamorphic basement lithologies. A provenance study has  
627 revealed that the age patterns of detrital zircons from the Ordovician - Devonian  
628 strata contain main age peaks at 430 - 445 Ma, 930 - 800 Ma, and 790 - 760  
629 Ma, with subordinate Neoproterozoic to Mesoproterozoic ages (Yan, 2022). Our  
630 results are consistent with this detrital zircon age information from the Lower  
631 Paleozoic sedimentary rocks and with the paleocurrent results of previous



632 studies (Wu et al., 2021). The findings from detrital zircon analyses are also  
633 compatible with the constraints from clast lithologies in the Lower Jurassic  
634 conglomerate, indicating a proximal feature of the source- to-sink system  
635 developed in the half grabens.

636 A Late Jurassic contractional event affected this region, as evidenced by  
637 the intense deformation and metamorphism displayed by various formations  
638 and rock units (Robinson et al., 2007; Groppo et al., 2019), and by the uplift  
639 and inversion of the earlier basin (Yang et al., 2017). The Middle Jurassic  
640 shallow marine sequences in Qiangtang and Pamir were uniformly eroded  
641 during this time period. The Upper Jurassic strata are either entirely absent or  
642 locally replaced by conglomerate deposits (Fig. 10). In the southern Tarim Basin,  
643 the Upper Jurassic strata are dominated by brownish reddish conglomerate of  
644 the Kuzigongsu Formation. Previous studies have suggested that these  
645 redbeds may have signalled a regional increase in aridity and the cessation of  
646 the monsoons as a result of the uplift of the surrounding mountain belts  
647 (Hendrix, 2000). A Late Jurassic uplift event, which significantly impacted the  
648 basinal tectonostratigraphy, has been corroborated by numerous  
649 thermochronologic ages (170-155 Ma) within the West Kunlun Mountains and  
650 Pamir (Fig.1c; Yang et al., 2017). The inferred uplift event also resulted in  
651 significant changes in basin and range patterns, and influenced the potential  
652 provenance of sediments. The emergence of juvenile detrital zircons in these  
653 Upper Jurassic and Lower Cretaceous deposits indicates the exhumation and  
654 erosion of a late Paleozoic to Mesozoic arc system (Fig. 10). The Triassic  
655 batholiths were thrust onto the southwestern margin of the Tarim Basin creating  
656 an elevated topography, which in turn provided abundant clastic material into



657 the Cretaceous depocenters in the region.

658

659 **6.3 Switching extensional and contractional tectonics related to the**  
660 **subduction of Neo-Tethys**

661 The Mesozoic era records the transition from the closure of the Paleo-  
662 Tethys Ocean to the initiation of subduction within Neo-Tethys (Wan et al., 2019).  
663 These processes are influenced by complex plate tectonic conditions, as the  
664 evolution of the Paleo- and Neo-Tethys Oceans varies significantly in their time-  
665 space patterns. The two Tethyan seaways diverge into several branches  
666 extending from Iran to Pamir, then eastward into the Tibetan Plateau (Fig. 1a).  
667 Deciphering the history of the Pamir Tethyan segment, therefore, improves our  
668 knowledge of the geodynamic evolution of the entire Tethyan realm.

669 Two major tectonic events profoundly affected the sedimentary patterns of  
670 the Mesozoic successions in this region. Episodic collisions along the southern  
671 Asian margin in the Late Triassic and then in the Late Jurassic resulted in major  
672 deformation (Jolivet, 2017). The regional magmatic history and the results of  
673 the provenance studies of the Jurassic basin necessitate a geodynamic  
674 scenario to explain the mechanism of an extensional tectonic event between  
675 two major contractional events. Although a flat subduction model has recently  
676 been proposed to explain the regional Cretaceous magmatism in the Pamir, the  
677 mode of Jurassic tectonic processes remains poorly constrained (Chapman et  
678 al., 2018). As discussed above, the history of the Neo-Tethyan subduction  
679 events significantly varies spatially. The initiation of subduction along the  
680 Tibetan margin occurred during the Middle Triassic, leading to volcanic  
681 activities in the southern Lhasa (Wang et al., 2016; Xie et al., 2021), whereas



682 the subduction in the Iran sector in the same orogenic belt farther west initiated  
683 later in the Early Jurassic (Wan et al., 2023). The extensive Early-Middle arc  
684 Jurassic magmatism along both continental margins indicates a synchronous  
685 flare-up of continental arcs (Fig. 11a and 11c). The bimodal volcanism (195-174  
686 Ma) in the Gangdese arc was associated with the subsequent opening of a  
687 back-arc basin (174-156 Ma) (Fig. 11c; Kapp and DeCelles, 2019). The  
688 magmatic arc of the Sanandaj–Sirjan belt (180-140 Ma) in SW Iran was  
689 facilitated by a simultaneous progressive back-arc rift (Fig. 11a; Hassanzadeh  
690 and Wernicke, 2016; Azizi and Stern, 2019).

691 By comparison, compiled magmatic detrital zircons in the Pamir segment  
692 reveal that Early-Middle Jurassic magmatism was almost absent there (Fig. 11b;  
693 Chapman et al., 2018). Available geochronological data indicate that Jurassic  
694 igneous rocks surrounding the Pamir are also limited, with only basalts exposed  
695 in the North Kunlun (Kandilik) and Tianshuihai regions (Jian et al., 2019) and  
696 bimodal volcanic rock suites found in the east of Karakoram (Zhou et al., 2019).  
697 Geochemical studies reveal that these coeval basaltic lavas (178-174 Ma)  
698 exhibit distinct features in their major and trace element compositions (Fig. 7  
699 and 8). Magmas of the basaltic lavas in the North Kunlun were dominated by  
700 within-plate basalts that shared similar compositions with typical OIB. In  
701 contrast, basalts in the Tianshuihai to the south were dominated by back-arc  
702 MORBs, characterized by distinct Nb-Ta depletions. The scarcity of zircon-rich  
703 felsic magmas in this region evidently differs from the conditions in the western  
704 and eastern segments of the Eurasian Tethyan margins where arc magmatism  
705 developed upon continental basement. To date, the exact timing of the onset of  
706 subduction-related magmatism in the Pamir Tethyan margin remains unclear.



707 The geochronological dataset for the Karakoram arc and the Kohistan Ladakh  
708 arc indicates that magmatic activity may have occurred as early as the Late  
709 Jurassic (Fig. 11b; Jagoutz et al., 2018; Saktura et al., 2023).

710 While the spatial continuity of the Tethyan suture zones from Iran into Tibet  
711 remains enigmatic, we propose that the regional Early to Middle Jurassic  
712 extension expressed across the southern Eurasian continental margin was a  
713 consequence of retreating subduction of the Neo-Tethyan Ocean floor. First,  
714 the transition from Cimmerian orogenic build-up (200-185 Ma) to large-scale  
715 continental extension (178-174 Ma) suggests the involvement of additional  
716 external extensional stresses, different from the classic cases of continent -  
717 continent collision (Weller et al., 2021). No typical post-collisional mafic igneous  
718 rock has been identified in the West Kunlun Orogenic Belt as of now. Secondly,  
719 the 195 Ma bimodal volcanic rocks in Karakoram and the 174 Ma MORB-like  
720 basalts in Tianshuihai have been suggested as associated with the initial  
721 opening of a back-arc basin, based on their geochemical signatures of crustal  
722 material metasomatism (Jian et al., 2019; Zhou et al., 2019). The magmatism  
723 in Pamir and Karakoram was quite similar to the extensional episodes that  
724 occurred in the southern margin of the Lhasa block, caused by accelerated slab  
725 rollback (Kapp and DeCelles, 2019). Thirdly, deposition of shallow marine  
726 carbonates was prevalent in the Pamir and Karakoram during the Middle  
727 Jurassic (Fig. 10), indicating an expansive extensional continental platform  
728 facing the ocean (Yang et al., 2017). These scenarios are analogous to the  
729 active margin of the western Pacific rim, which is characterized by a broad  
730 marginal sea with an outboard trench - subduction chain (Fig. 1a). Additionally,  
731 the Middle Jurassic extension occurred across the broad hinterlands of central



732 Asia, which cannot be easily explained by the collapse of the Paleo-Tethyan  
733 orogenic belt (Otto, 1997).

734 During the Late Jurassic, this marginal extensional basin started to invert,  
735 with extensive contractional deformation of the Lower-Middle Jurassic  
736 carbonate strata and the development of a major angular unconformity (Gaetani  
737 et al., 1993; Robinson, 2015). Available basement thermochronological data  
738 show widespread exhumation across the West Kunlun Mountains (Fig. 1c), as  
739 well as the reactivation of the Paleo-Tethyan sutures within the Pamir terranes  
740 (Schwab et al., 2004). The exhumation of the Triassic plutons in the South  
741 Kunlun Mountain led to the transport of debris material from the magmatic arc  
742 into the Tarim basin through braided fluvial network systems (Fig. 11b). This  
743 broad uplift event has been interpreted as retro-arc deformation and shortening  
744 related to the advancing subduction of the Neo-Tethyan Ocean (Robinson,  
745 2015).

746 The subduction style along the broader strike-length of the Tethyan orogen  
747 varied from the west to the east in the Late Jurassic - Early Cretaceous. Similar  
748 to the West Kunlun Mountains, the Lhasa block to the east experienced basin  
749 inversion and contractional deformation starting by ca. 155 Ma and throughout  
750 the Early Cretaceous (e.g., Murphy et al., 1997; Ding and Lai, 2003; Kapp and  
751 DeCelles, 2019). Geological mapping has documented significant shortening  
752 strain (~ 60%) across Lhasa at this time (Murphy et al., 1997). Although the  
753 cause of this event has been debated, the magmatic lull since the earliest  
754 Cretaceous and subsequent flare-up in the Mid-Cretaceous in both regions  
755 imply that they shared a similar geodynamic setting (Fig. 11; Chapman et al.,  
756 2018). Conversely, the Iranian segment to the west experienced continuous



757 extension at the same time (Hunziker et al., 2015; Lechmann et al., 2018;  
758 Maghdour-Mashhour et al., 2021). These along-strike variations likely reflect  
759 broad geodynamic changes to, or initial conditions of, the Tethyan Ocean  
760 system that warrant future investigations. For example, variable plate  
761 convergence rates related to global tectonic configurations or the oceanic-plate  
762 age variations could result in unique tectonic events along the strike-length of  
763 the entire Tethyan orogen. Alternatively, the closure of the Bangong-Nujiang  
764 Ocean, another branch of the Tethyan system between the Lhasa and  
765 Qiangtang blocks, might have also played a significant role in along-strike  
766 variations within the Tethyan orogenic belt (Fig. 11; Yang et al., 2017; Kapp and  
767 DeCelles, 2019).

768

## 769 **7 Conclusion**

770 This study has concentrated on the stratigraphy and provenance of  
771 Jurassic strata in the West Kunlun Mountains to better understand the  
772 Mesozoic geological evolution of the Eurasian margin within the framework of  
773 the Tethyan geodynamics. Our investigations of the Jurassic sedimentary  
774 successions, combined with new geochronological and geochemical data from  
775 coeval basaltic lava intercalations, led to the following conclusions:

776 (1) A newly identified, thick sedimentary package with basaltic lava  
777 interlayers in the southern end of the Kyzyltau basin bears similarities to the  
778 Lower and Middle Jurassic sequences in their clastic compositions and  
779 structures. Zircon U-Pb dating results from basaltic lavas suggest an Early  
780 Jurassic age (~ 178 Ma) for this stratigraphic member, in contrast to a  
781 Precambrian age previously reported. This is a significant change that strongly





782 affects the current tectonic interpretations and models.

783 (2) Our new geochemical data from the Early Jurassic basaltic extrusive  
784 rocks show that magmas of these basalts had typical OIB affinities, and that  
785 they lacked crustal contamination. Thus, the related magmatism likely occurred  
786 in an intraplate rifting setting and was facilitated by extensional fault systems,  
787 which significantly reduced the residence time of the ascending magmas in the  
788 crust avoiding contamination.

789 (3) Provenance analysis, integrating conglomerate clast lithologies with  
790 detrital zircons, indicates a significant source contribution from local basements  
791 (North Kunlun) for the Early to Middle Jurassic rift basins. In comparison, the  
792 Late Jurassic contractional event caused an uplift of the surrounding mountains  
793 in the South Kunlun and Pamir, significantly influencing the basin  
794 tectonostratigraphy and source- to -sink system.

795 (4) The alternating extensional and contractional tectonic episodes in the  
796 West Kunlun Mountains and a wider region across the southern Eurasian  
797 margin are related to changes in the subduction style of the Neo-Tethyan Ocean  
798 floor, transitioning from retreating in Early - Middle Jurassic to advancing in Late  
799 Jurassic - Early Cretaceous.

800

#### 801 **Declaration of Competing Interest**

802 The authors declare that they have no known competing financial interests  
803 or personal relationships that could have appeared to influence the work  
804 reported in this paper.

805



806 **Acknowledgement**

807 This work was supported by the National Natural Science Foundation of  
808 China (Grants No. U22B6002 and 42302231). H.-X. Wu received the funding  
809 of Postdoctoral Science Foundation (2023M742979).

810

811 **Author Contributions**

812 *Hong-Xiang Wu*: Conceptualization, Formal Analysis, Investigation,  
813 Methodology, Visualization, Writing – original draft, Writing – review & editing,  
814 Funding acquisition; *Han-Lin Chen*: Funding acquisition, Investigation, Project  
815 administration; *Andrew V. Zuza*: Writing – review & editing; *Yildirim Dilek*:  
816 Writing – review & editing; *Du-Wei Qiu*: Investigation, Formal Analysis; *Qi-Ye*  
817 *Lu*: Investigation, Formal Analysis; *Feng-Qi Zhang*: Investigation, Formal  
818 Analysis; *Xiao-Gan Cheng*: Investigation; *Xiu-Bin Lin*: Investigation.

819

820 **Data availability**

821 The data used in this study are available in the references and  
822 Supplementary Material, including five tables and one figure.

823



824 **References**

- 825 Aldanmaz, E., Pearce, J. A., Thirlwall, M. F., and Mitchell, J. G.: Petrogenetic  
826 evolution of late Cenozoic, post-collision volcanism in western Anatolia,  
827 Turkey, *Journal of Volcanology and Geothermal Research*, 102, 67-95,  
828 [https://doi.org/10.1016/S0377-0273\(00\)00182-7](https://doi.org/10.1016/S0377-0273(00)00182-7), 2000.
- 829 Andersen, T.: Correction of common lead in U–Pb analyses that do not report  
830  $^{204}\text{Pb}$ , *Chemical Geology*, 192, 59-79, [https://doi.org/10.1016/S0009-2541\(02\)00195-X](https://doi.org/10.1016/S0009-2541(02)00195-X), 2002.
- 832 Angiolini, L., Zanchi, A., Zanchetta, S., Nicora, A., Vuolo, I., Berra, F.,  
833 Henderson, C., Malaspina, N., Rettori, R., Vachard, D., and Vezzoli, G.:  
834 From rift to drift in South Pamir (Tajikistan): Permian evolution of a  
835 Cimmerian terrane, *Journal of Asian Earth Sciences*, 102, 146-169,  
836 <https://doi.org/10.1016/j.jseaes.2014.08.001>, 2015.
- 837 Angiolini, L., Zanchi, A., Zanchetta, S., Nicora, A., and Vezzoli, G.: The  
838 Cimmerian geopuzzle: new data from South Pamir, *Terra Nova*, 25, 352-  
839 360, <https://doi.org/10.1111/ter.12042>, 2013.
- 840 Aitchison, S. J. and Forrest, A. H.: Quantification of Crustal Contamination in  
841 Open Magmatic Systems, *Journal of Petrology*, 35, 461-488,  
842 [10.1093/petrology/35.2.461](https://doi.org/10.1093/petrology/35.2.461), 1994.
- 843 Azizi, H. and Stern, R. J.: Jurassic igneous rocks of the central Sanandaj–Sirjan  
844 zone (Iran) mark a propagating continental rift, not a magmatic arc, *Terra*  
845 *Nova*, 31, 415-423, <https://doi.org/10.1111/ter.12404>, 2019.
- 846 Belousova, E., Griffin, W., O'Reilly, S. Y., and Fisher, N.: Igneous zircon: trace  
847 element composition as an indicator of source rock type, *Contributions to*  
848 *Mineralogy and Petrology*, 143, 602-622, [10.1007/s00410-002-0364-7](https://doi.org/10.1007/s00410-002-0364-7),



- 849           2002.
- 850 Brookfield, M. E. and Hashmat, A.: The geology and petroleum potential of the  
851           North Afghan platform and adjacent areas (northern Afghanistan, with parts  
852           of southern Turkmenistan, Uzbekistan and Tajikistan), *Earth-Science*  
853           Reviews, 55, 41-71, [https://doi.org/10.1016/S0012-8252\(01\)00036-8](https://doi.org/10.1016/S0012-8252(01)00036-8),  
854           2001.
- 855 Burtman, V. S. and Molnar, P.: Geological and Geophysical Evidence for Deep  
856           Subduction of Continental Crust Beneath the Pamir, in: *Geological and*  
857           Geophysical Evidence for Deep Subduction of Continental Crust Beneath  
858           the Pamir, Geological Society of America, 0, 10.1130/SPE281-p1, 1993.
- 859 Cabanis, B. and Lecolle, M.: The La/10-Y/15-Nb/8 diagram: a tool for  
860           discriminating volcanic series and evidencing continental crust magmatic  
861           mixtures and/or contamination, *Comptes Rendus - Academie des*  
862           Sciences, Serie II, 309, 2023-2029, 1989.
- 863 Cao, K., Wang, G.-C., Bernet, M., van der Beek, P., and Zhang, K.-X.:  
864           Exhumation history of the West Kunlun Mountains, northwestern Tibet:  
865           Evidence for a long-lived, rejuvenated orogen, *Earth and Planetary*  
866           Science Letters, 432, 391-403, <https://doi.org/10.1016/j.epsl.2015.10.033>,  
867           2015.
- 868 Cao, W., Zahirovic, S., Flament, N., Williams, S., Golonka, J., and Müller, R. D.:  
869           Improving global paleogeography since the late Paleozoic using  
870           paleobiology, *Biogeosciences*, 14, 5425-5439, 10.5194/bg-14-5425-2017,  
871           2017.
- 872 Chapman, J. B., Scoggin, S. H., Kapp, P., Carrapa, B., Ducea, M. N.,  
873           Worthington, J., Oimahmadov, I., and Gadoev, M.: Mesozoic to Cenozoic



- 874 magmatic history of the Pamir, *Earth and Planetary Science Letters*, 482,  
875 181-192, <https://doi.org/10.1016/j.epsl.2017.10.041>, 2018.
- 876 Chen, S., Chen, H., Zhu, K., and Tao, Y.: Petrogenesis of the Middle–Late  
877 Triassic S- and I-type granitoids in the eastern Pamir and implications for  
878 the Tanymas–Jinshajiang Paleo-Tethys Ocean, *International Journal of*  
879 *Earth Sciences*, 110, 1213-1232, [10.1007/s00531-021-02013-z](https://doi.org/10.1007/s00531-021-02013-z), 2021.
- 880 Chen, Y., Wu, H., Zhang, L., Cheng, X., Chen, C., Zhang, Y., Ren, P., Zhang, F.,  
881 and Chen, H.: Characteristics of the Late Triassic paleo-structure in the  
882 mountain front region of western Kunlun and its control of Jurassic–  
883 Cretaceous deposition, *Chinese Journal of Geology*, 53, 1405-1418, 2018  
884 (in Chinese with English abstract).
- 885 Corfu, F., Hanchar, J. M., Hoskin, P. W. O., and Kinny, P.: Atlas of Zircon  
886 Textures, *Reviews in Mineralogy and Geochemistry*, 53, 469-500,  
887 [10.2113/0530469](https://doi.org/10.2113/0530469), 2003.
- 888 Cowgill, E.: Cenozoic right-slip faulting along the eastern margin of the Pamir  
889 salient, northwestern China, *GSA Bulletin*, 122, 145-161,  
890 [10.1130/b26520.1](https://doi.org/10.1130/b26520.1), 2010.
- 891 Dewey, J. F.: Orogeny can be very short, *Proceedings of the National Academy*  
892 *of Sciences*, 102, 15286-15293, [doi:10.1073/pnas.0505516102](https://doi.org/10.1073/pnas.0505516102), 2005.
- 893 Dilek, Y. and Altunkaynak, Ş.: Cenozoic Crustal Evolution and Mantle Dynamics  
894 of Post-Collisional Magmatism in Western Anatolia, *International Geology*  
895 *Review*, 49, 431-453, [10.2747/0020-6814.49.5.431](https://doi.org/10.2747/0020-6814.49.5.431), 2007.
- 896 Dilek, Y. and Altunkaynak, Ş.: Geochemistry of Neogene–Quaternary alkaline  
897 volcanism in western Anatolia, Turkey, and implications for the Aegean  
898 mantle, *International Geology Review*, 52, 631-655,



- 899           10.1080/00206810903495020, 2010.
- 900   Dilek, Y. and Furnes, H.: Tethyan ophiolites and Tethyan seaways, *Journal of*  
901           the Geological Society, 176, 899-912, doi:10.1144/jgs2019-129, 2019.
- 902   Dilek, Y. and Moores, E. M.: Regional tectonics of the eastern Mediterranean  
903           ophiolites. In: J. Malpas, E. M. Moores, A. Panayiotou, and C. Xenophontos  
904           (Eds), *Ophiolites. Oceanic Crustal Analogues, Proceedings of the*  
905           Symposium "Troodos 1987", The Geological Survey Department, Nicosia,  
906           Cyprus, 295–309, 1990.
- 907   Ding, L. and Lai, Q.: New geological evidence of crustal thickening in the  
908           Gangdese block prior to the Indo-Asian collision, *Chinese Science Bulletin*,  
909           48, 1604-1610, 10.1007/BF03183969, 2003.
- 910   Dong, Y., He, D., Sun, S., Liu, X., Zhou, X., Zhang, F., Yang, Z., Cheng, B.,  
911           Zhao, G., and Li, J.: Subduction and accretionary tectonics of the East  
912           Kunlun orogen, western segment of the Central China Orogenic System,  
913           *Earth-Science Reviews*, 186, 231-261,  
914           <https://doi.org/10.1016/j.earscirev.2017.12.006>, 2018.
- 915   Faisal, S., Larson, K. P., Cottle, J. M., and Lamming, J.: Building the Hindu Kush:  
916           monazite records of terrane accretion, plutonism and the evolution of the  
917           Himalaya–Karakoram–Tibet orogen, *Terra Nova*, 26, 395-401,  
918           <https://doi.org/10.1111/ter.12112>, 2014.
- 919   Fürsich, F. T., Brunet, M.-F., Auxièrre, J.-L., and Munsch, H.: Lower–Middle  
920           Jurassic facies patterns in the NW Afghan–Tajik Basin of southern  
921           Uzbekistan and their geodynamic context, in: *Geological Evolution of*  
922           Central Asian Basins and the Western Tien Shan Range, edited by: Brunet,  
923           M. F., McCann, T., and Sobel, E. R., Geological Society of London, 0,



- 924 10.1144/sp427.9, 2017.
- 925 Gaetani, M., Jadoul, F., Erba, E., and Garzanti, E.: Jurassic and Cretaceous  
926 orogenic events in the North Karakoram: age constraints from sedimentary  
927 rocks, Geological Society, London, Special Publications, 74, 39-52,  
928 doi:10.1144/GSL.SP.1993.074.01.04, 1993.
- 929 Golonka, J.: Plate tectonic evolution of the southern margin of Eurasia in the  
930 Mesozoic and Cenozoic, Tectonophysics, 381, 235-273,  
931 <https://doi.org/10.1016/j.tecto.2002.06.004>, 2004.
- 932 Groppo, C., Rolfo, F., McClelland, W. C., and Coble, M. A.: Pre-Cenozoic  
933 evolution of the Aghil Range (western Tibetan Plateau): A missing piece of  
934 the Tibet-Pamir-Karakorum geopuzzle, Gondwana Research, 69, 122-143,  
935 <https://doi.org/10.1016/j.gr.2018.12.006>, 2019.
- 936 Guo, P., Niu, Y., Sun, P., Gong, H., and Wang, X.: Lithosphere thickness  
937 controls continental basalt compositions: An illustration using Cenozoic  
938 basalts from eastern China, Geology, 48, 128-133, 10.1130/g46710.1,  
939 2020.
- 940 Harris, N. B. W., Pearce, J. A., and Tindle, A. G.: Geochemical characteristics  
941 of collision-zone magmatism, Geological Society, London, Special  
942 Publications, 19, 67-81, doi:10.1144/GSL.SP.1986.019.01.04, 1986.
- 943 Hassanzadeh, J. and Wernicke, B. P.: The Neotethyan Sanandaj-Sirjan zone  
944 of Iran as an archetype for passive margin-arc transitions, Tectonics, 35,  
945 586-621, <https://doi.org/10.1002/2015TC003926>, 2016.
- 946 Hendrix, M. S.: Evolution of Mesozoic Sandstone Compositions, Southern  
947 Junggar, Northern Tarim, and Western Turpan Basins, Northwest China: A  
948 Detrital Record of the Ancestral Tian Shan, Journal of Sedimentary



- 949 Research, 70, 520-532, doi:10.1306/2dc40924-0e47-11d7-  
950 8643000102c1865d, 2000.
- 951 Hendrix, M. S., Graham, S. A., Carroll, A. R., Sobel, E. R., McKnight, C. L.,  
952 Schulein, B. J., and Wang, Z.: Sedimentary record and climatic implications  
953 of recurrent deformation in the Tian Shan: Evidence from Mesozoic strata  
954 of the north Tarim, south Junggar, and Turpan basins, northwest China,  
955 GSA Bulletin, 104, 53-79, 10.1130/0016-  
956 7606(1992)104<0053:Scacio>2.3.Co;2, 1992.
- 957 Hoskin, P. W. O. and Schaltegger, U.: The Composition of Zircon and Igneous  
958 and Metamorphic Petrogenesis, Reviews in Mineralogy and Geochemistry,  
959 53, 27-62, 10.2113/0530027, 2003.
- 960 Hunziker, D., Burg, J.-P., Bouilhol, P., and von Quadt, A.: Jurassic rifting at the  
961 Eurasian Tethys margin: Geochemical and geochronological constraints  
962 from granitoids of North Makran, southeastern Iran, Tectonics, 34, 571-593,  
963 <https://doi.org/10.1002/2014TC003768>, 2015.
- 964 Hou, Z., Duan, L., Lu, Y., Zheng, Y., Zhu, D., Yang, Z., Yang, Z., Wang, B., Pei,  
965 Y., Zhao, Z., and McCuaig, T. C.: Lithospheric Architecture of the Lhasa  
966 Terrane and Its Control on Ore Deposits in the Himalayan-Tibetan Orogen\*,  
967 Economic Geology, 110, 1541-1575, 10.2113/econgeo.110.6.1541, 2015.
- 968 Jafari, A., Ao, S., Jamei, S., and Ghasemi, H.: Evolution of the Zagros sector of  
969 Neo-Tethys: Tectonic and magmatic events that shaped its rifting, seafloor  
970 spreading and subduction history, Earth-Science Reviews, 241, 104419,  
971 <https://doi.org/10.1016/j.earscirev.2023.104419>, 2023.
- 972 Jagoutz, O., Bouilhol, P., Schaltegger, U., and Müntener, O.: The isotopic  
973 evolution of the Kohistan Ladakh arc from subduction initiation to continent





- 974 arc collision, in: *Himalayan Tectonics: A Modern Synthesis*, edited by:  
975 Treloar, P. J., and Searle, M. P., The Geological Society of London, 0,  
976 10.1144/sp483.7, 2019.
- 977 Jian, K., Gao, F., Du, B., Zhang, Z., Wang, X., and Zhao, D.: Formation age,  
978 geochemical characteristics and tectonic setting of the basalts from  
979 Longshan Formation in Heweitai area, Karakorum, *J Mineral Petrol*, 39,  
980 42-51, 2019 (in Chinese with English abstract).
- 981 Jolivet, M.: Mesozoic tectonic and topographic evolution of Central Asia and  
982 Tibet: a preliminary synthesis, Geological Society, London, Special  
983 Publications, 427, 19-55, doi:10.1144/SP427.2, 2017.
- 984 Kapp, P. and DeCelles, P. G.: Mesozoic–Cenozoic Geological Evolution of the  
985 Himalayan-Tibetan Orogen and Working Tectonic Hypotheses, *American*  
986 *Journal of Science*, 319, 159-+, 10.2475/03.2019.01, 2019.
- 987 Kapp, P., DeCelles, P. G., Gehrels, G. E., Heizler, M., and Ding, L.: Geological  
988 records of the Lhasa-Qiangtang and Indo-Asian collisions in the Nima area  
989 of central Tibet, *GSA Bulletin*, 119, 917-933, 10.1130/b26033.1, 2007.
- 990 Kazmin, V. G.: Collision and rifting in the Tethys Ocean: geodynamic implication,  
991 *Tectonophysics*, 196, 371-384, [https://doi.org/10.1016/0040-](https://doi.org/10.1016/0040-1951(91)90331-L)  
992 1951(91)90331-L, 1991.
- 993 Krienitz, M. S., Haase, K. M., Mezger, K., Eckardt, V., and Shaikh-Mashail, M.  
994 A.: Magma genesis and crustal contamination of continental intraplate  
995 lavas in northwestern Syria, *Contributions to Mineralogy and Petrology*,  
996 151, 698-716, 10.1007/s00410-006-0088-1, 2006.
- 997 Lechmann, A., Burg, J.-P., Ulmer, P., Mohammadi, A., Guillong, M., and Faridi,  
998 M.: From Jurassic rifting to Cretaceous subduction in NW Iranian



- 999 Azerbaijan: geochronological and geochemical signals from granitoids,  
1000 Contributions to Mineralogy and Petrology, 173, 102, 10.1007/s00410-018-  
1001 1532-8, 2018.
- 1002 Leith, W.: A mid-Mesozoic extension across Central Asia?, Nature, 313, 567-  
1003 570, 10.1038/313567a0, 1985.
- 1004 Li, G., Sandiford, M., Fang, A., Kohn, B., Sandiford, D., Fu, B., Zhang, T., Cao,  
1005 Y., and Chen, F.: Multi-stage exhumation history of the West Kunlun orogen  
1006 and the amalgamation of the Tibetan Plateau, Earth and Planetary Science  
1007 Letters, 528, 115833, <https://doi.org/10.1016/j.epsl.2019.115833>, 2019.
- 1008 Li, L., Najman, Y., Dupont-Nivet, G., Parra, M., Roperch, P., Kaya, M., Meijer,  
1009 N., O'Sullivan, P., Jepson, G., and Aminov, J.: Mesozoic–Cenozoic  
1010 multistage tectonic evolution of the Pamir: Detrital fission-track constraints  
1011 from the Tajik Basin, Basin Research, 35, 530-550,  
1012 <https://doi.org/10.1111/bre.12721>, 2023.
- 1013 Li, S., Zhao, S., Liu, X., Cao, H., Yu, S., Li, X., Somerville, I., Yu, S., and Suo,  
1014 Y.: Closure of the Proto-Tethys Ocean and Early Paleozoic amalgamation  
1015 of microcontinental blocks in East Asia, Earth-Science Reviews, 186, 37-  
1016 75, <https://doi.org/10.1016/j.earscirev.2017.01.011>, 2018.
- 1017 Li, Y., Robinson, A. C., Zucali, M., Gadoev, M., Oimhammadzoda, I., Lapen, T.  
1018 J., and Carrapa, B.: Mesozoic Tectonic Evolution in the Kurgovat-Vanch  
1019 Complex, NW Pamir, Tectonics, 41, e2021TC007180,  
1020 <https://doi.org/10.1029/2021TC007180>, 2022b.
- 1021 Li, Y., Wen, L., Yang, X.-Z., Li, C., Zhang, L., Wang, B., Chen, C., Liu, Y.-L., and  
1022 Li, Y.-J.: Mesozoic Collision-Related Structures in the Southern Tarim  
1023 Basin, W. China: Implications for the Paleo-Tethys Closing Process,



- 1024           Frontiers in Earth Science, 9, 10.3389/feart.2021.792049, 2022a.
- 1025   Liao, S., Jiang, Y., Zhou, Q., Yang, W., Jin, G., and Zhao, P.: Geochemistry and  
1026           geodynamic implications of the Triassic bimodal magmatism from Western  
1027           Kunlun Orogen, northwest China, International Journal of Earth Sciences,  
1028           101, 555-577, 10.1007/s00531-011-0686-7, 2012.
- 1029   Ma, S., Wang, Y., and Fang, X.: Basic characteristics of Proterozoic Eonothem  
1030           as a table cover on northern slope, Xinjiang Geology, 9, 59-71, 1991 (in  
1031           Chinese with English abstract).
- 1032   Ma, X., Xu, Z., Meert, J., and Santosh, M.: Early Jurassic intra-oceanic arc  
1033           system of the Neotethys Ocean: Constraints from andesites in the  
1034           Gangdese magmatic belt, south Tibet, Island Arc, 26, e12202,  
1035           <https://doi.org/10.1111/iar.12202>, 2017.
- 1036   Maghdour-Mashhour, R., Hayes, B., Pang, K.-N., Bolhar, R., Tabbakh Shabani,  
1037           A. A., and Elahi-Janatmakan, F.: Episodic subduction initiation triggered  
1038           Jurassic magmatism in the Sanandaj–Sirjan zone, Iran, Lithos, 396-397,  
1039           106189, <https://doi.org/10.1016/j.lithos.2021.106189>, 2021.
- 1040   Mattern, F. and Schneider, W.: Suturing of the Proto- and Paleo-Tethys oceans  
1041           in the western Kunlun (Xinjiang, China), Journal of Asian Earth Sciences,  
1042           18, 637-650, [https://doi.org/10.1016/S1367-9120\(00\)00011-0](https://doi.org/10.1016/S1367-9120(00)00011-0), 2000.
- 1043   Meschede, M.: A method of discriminating between different types of mid-ocean  
1044           ridge basalts and continental tholeiites with the Nb 1bZr 1bY diagram,  
1045           Chemical Geology, 56, 207-218, [https://doi.org/10.1016/0009-](https://doi.org/10.1016/0009-2541(86)90004-5)  
1046           2541(86)90004-5, 1986.
- 1047   Metcalf, I.: Gondwana dispersion and Asian accretion: Tectonic and  
1048           palaeogeographic evolution of eastern Tethys, Journal of Asian Earth



- 1049 Sciences, 66, 1-33, 10.1016/j.jseas.2012.12.020, 2013.
- 1050 Metcalfe, I.: Multiple Tethyan ocean basins and orogenic belts in Asia,  
1051 Gondwana Research, 100, 87-130,  
1052 <https://doi.org/10.1016/j.gr.2021.01.012>, 2021.
- 1053 Middlemost, E. A. K.: Naming materials in the magma/igneous rock system,  
1054 Earth-Science Reviews, 37, 215-224, [https://doi.org/10.1016/0012-8252\(94\)90029-9](https://doi.org/10.1016/0012-8252(94)90029-9), 1994.
- 1056 Murphy, M. A., Yin, A., Harrison, T. M., Dürr, S. B., Z, C., Ryerson, F. J., Kidd,  
1057 W. S. F., X, W., and X, Z.: Did the Indo-Asian collision alone create the  
1058 Tibetan plateau?, Geology, 25, 719-722, 10.1130/0091-  
1059 7613(1997)025<0719:Dtiaca>2.3.Co;2, 1997.
- 1060 Otto, S. C.: Mesozoic-Cenozoic history of deformation and petroleum systems  
1061 in sedimentary basins of Central Asia; implications of collisions on the  
1062 Eurasian margin, Petroleum Geoscience, 3, 327-341,  
1063 10.1144/petgeo.3.4.327, 1997.
- 1064 Pearce, J. A.: Geochemical fingerprinting of oceanic basalts with applications  
1065 to ophiolite classification and the search for Archean oceanic crust, Lithos,  
1066 100, 14-48, <https://doi.org/10.1016/j.lithos.2007.06.016>, 2008.
- 1067 Pearce, J. A.: Trace element characteristics of lavas from destructive plate  
1068 boundaries, in: Orogenic Andesites and Related Rocks, edited by: Thorpe,  
1069 R. S., John Wiley and Sons, Chichester, England, 525-548, 1982.
- 1070 Qu, J., Zhang, L., Zhang, J., and Zhang, B.: Petrology and geochronology on  
1071 high-pressure pelitic granulite from Bulunkuole complex in West Kunlun  
1072 and its tectonic implication, Acta Petrologica Siniaca, 37, 563-574,  
1073 10.18654/1000-0569/2021.02.14, 2021.



- 1074 Robinson, A. C.: Mesozoic tectonics of the Gondwanan terranes of the Pamir  
1075 plateau, *Journal of Asian Earth Sciences*, 102, 170-179,  
1076 <https://doi.org/10.1016/j.jseaes.2014.09.012>, 2015.
- 1077 Robinson, A. C., Yin, A., Manning, C. E., Harrison, T. M., Zhang, S.-H., and  
1078 Wang, X.-F.: Cenozoic evolution of the eastern Pamir: Implications for  
1079 strain-accommodation mechanisms at the western end of the Himalayan-  
1080 Tibetan orogen, *GSA Bulletin*, 119, 882-896, 10.1130/b25981.1, 2007.
- 1081 Rollinson, H. R.: *Using Geochemical Data: Evaluation, Presentation,*  
1082 *Interpretation*, Mineralogical Magazine, Longman, Edinburgh Gate,  
1083 London, 352 pp.1993.
- 1084 Ruban, D. A., Al-Husseini, M. I., and Iwasaki, Y.: Review of Middle East  
1085 Paleozoic plate tectonics, *GeoArabia*, 12, 35-56,  
1086 [10.2113/geoarabia120335](https://doi.org/10.2113/geoarabia120335), 2007.
- 1087 Saktura, W. M., Buckman, S., Nutman, A. P., Walsh, J., and Murray, G.:  
1088 Magmatic records from the Karakoram terrane: U–Pb zircon ages from  
1089 granites and modern sediments in the Nubra Valley, NW Himalaya, *Journal*  
1090 *of Asian Earth Sciences*, 255, 105771,  
1091 <https://doi.org/10.1016/j.jseaes.2023.105771>, 2023.
- 1092 Schwab, M., Ratschbacher, L., Siebel, W., McWilliams, M., Minaev, V., Lutkov,  
1093 V., Chen, F., Stanek, K., Nelson, B., Frisch, W., and Wooden, J. L.:  
1094 Assembly of the Pamirs: Age and origin of magmatic belts from the  
1095 southern Tien Shan to the southern Pamirs and their relation to Tibet,  
1096 *Tectonics*, 23, <https://doi.org/10.1029/2003TC001583>, 2004.
- 1097 Şengör, A. M. C.: Mid-Mesozoic closure of Permo–Triassic Tethys and its  
1098 implications, *Nature*, 279, 590-593, 10.1038/279590a0, 1979.



- 1099 Şengör, A. M. C.: The Cimmeride Orogenic System and the Tectonics of  
1100 Eurasia, in: The Cimmeride Orogenic System and the Tectonics of Eurasia,  
1101 Geological Society of America, 0, 10.1130/SPE195-p1, 1984.
- 1102 Şengör, A. M. C.: Tectonics of the Tethysides: Orogenic Collage Development  
1103 in a Collisional Setting, Annual Review of Earth and Planetary Sciences,  
1104 15, 213-244, <https://doi.org/10.1146/annurev.ea.15.050187.001241>, 1987.
- 1105 Şengör, A. M. C., Altıner, D., Cin, A., Ustaömer, T., and Hsü, K. J.: Origin and  
1106 assembly of the Tethyside orogenic collage at the expense of Gondwana  
1107 Land, Geological Society, London, Special Publications, 37, 119-181,  
1108 doi:10.1144/GSL.SP.1988.037.01.09, 1988.
- 1109 Sobel, E. R.: Basin analysis of the Jurassic–Lower Cretaceous southwest Tarim  
1110 basin, northwest China, GSA Bulletin, 111, 709-724, 10.1130/0016-  
1111 7606(1999)111<0709:Baotjl>2.3.Co;2, 1999.
- 1112 Sobel, E. R., Chen, J., Schoenbohm, L. M., Thiede, R., Stockli, D. F., Sudo, M.,  
1113 and Strecker, M. R.: Oceanic-style subduction controls late Cenozoic  
1114 deformation of the Northern Pamir orogen, Earth and Planetary Science  
1115 Letters, 363, 204-218, <https://doi.org/10.1016/j.epsl.2012.12.009>, 2013.
- 1116 Stampfli, G., Marcoux, J., and Baud, A.: Tethyan margins in space and time,  
1117 Palaeogeography, Palaeoclimatology, Palaeoecology, 87, 373-409,  
1118 [https://doi.org/10.1016/0031-0182\(91\)90142-E](https://doi.org/10.1016/0031-0182(91)90142-E), 1991.
- 1119 Stampfli, G. M.: Tethyan oceans, Geological Society, London, Special  
1120 Publications, 173, 1-23, doi:10.1144/GSL.SP.2000.173.01.01, 2000.
- 1121 Stampfli, G. M. and Borel, G. D.: A plate tectonic model for the Paleozoic and  
1122 Mesozoic constrained by dynamic plate boundaries and restored synthetic  
1123 oceanic isochrons, Earth and Planetary Science Letters, 196, 17-33,



- 1124 [https://doi.org/10.1016/S0012-821X\(01\)00588-X](https://doi.org/10.1016/S0012-821X(01)00588-X), 2002.
- 1125 Sun, S.-S. and McDonough, W. F.: Chemical and isotopic systematics of  
1126 oceanic basalts: implications for mantle composition and processes,  
1127 Geological Society, London, Special Publications, 42, 313-345,  
1128 doi:10.1144/GSL.SP.1989.042.01.19, 1989.
- 1129 Tapponnier, P., Mattauer, M., Proust, F., and Cassaigneau, C.: Mesozoic  
1130 ophiolites, sutures, and large-scale tectonic movements in Afghanistan,  
1131 Earth and Planetary Science Letters, 52, 355-371,  
1132 [https://doi.org/10.1016/0012-821X\(81\)90189-8](https://doi.org/10.1016/0012-821X(81)90189-8), 1981.
- 1133 Tao, Z., Yin, J., Spencer, C. J., Sun, M., Xiao, W., Kerr, A. C., Wang, T., Huangfu,  
1134 P., Zeng, Y., and Chen, W.: Subduction polarity reversal facilitated by plate  
1135 coupling during arc-continent collision: Evidence from the Western Kunlun  
1136 orogenic belt, northwest Tibetan Plateau, *Geology*, 10.1130/g51847.1,  
1137 2024.
- 1138 Vermeesch, P.: IsoplotR: A free and open toolbox for geochronology,  
1139 *Geoscience Frontiers*, 9, 1479-1493,  
1140 <https://doi.org/10.1016/j.gsf.2018.04.001>, 2018.
- 1141 Vermeesch, P.: On the visualisation of detrital age distributions, *Chemical*  
1142 *Geology*, 312-313, 190-194,  
1143 <https://doi.org/10.1016/j.chemgeo.2012.04.021>, 2012.
- 1144 Wan, B., Chu, Y., Chen, L., Zhang, Z., Ao, S., and Talebian, M.: When and Why  
1145 the NeoTethyan Subduction Initiated Along the Eurasian Margin, in:  
1146 *Compressional Tectonics*, 245-260,  
1147 <https://doi.org/10.1002/9781119773856.ch9>, 2023.
- 1148 Wan, B., Wu, F., Chen, L., Zhao, L., Liang, X., Xiao, W., and Zhu, R.: Cyclical



- 1149 one-way continental rupture-drift in the Tethyan evolution: Subduction-  
1150 driven plate tectonics, *Science China Earth Sciences*, 62, 2005-2016,  
1151 10.1007/s11430-019-9393-4, 2019.
- 1152 Wang, C., Ding, L., Zhang, L.-Y., Kapp, P., Pullen, A., and Yue, Y.-H.:  
1153 Petrogenesis of Middle–Late Triassic volcanic rocks from the Gangdese  
1154 belt, southern Lhasa terrane: Implications for early subduction of Neo-  
1155 Tethyan oceanic lithosphere, *Lithos*, 262, 320-333,  
1156 <https://doi.org/10.1016/j.lithos.2016.07.021>, 2016.
- 1157 Wang, Y., Qian, X., Cawood, P. A., Liu, H., Feng, Q., Zhao, G., Zhang, Y., He,  
1158 H., and Zhang, P.: Closure of the East Paleotethyan Ocean and  
1159 amalgamation of the Eastern Cimmerian and Southeast Asia continental  
1160 fragments, *Earth-Science Reviews*, 186, 195-230,  
1161 <https://doi.org/10.1016/j.earscirev.2017.09.013>, 2018.
- 1162 Wei, Y., Zhao, Z., Niu, Y., Zhu, D.-C., Liu, D., Wang, Q., Hou, Z., Mo, X., and  
1163 Wei, J.: Geochronology and geochemistry of the Early Jurassic Yeba  
1164 Formation volcanic rocks in southern Tibet: Initiation of back-arc rifting and  
1165 crustal accretion in the southern Lhasa Terrane, *Lithos*, 278-281, 477-490,  
1166 <https://doi.org/10.1016/j.lithos.2017.02.013>, 2017.
- 1167 Weller, O. M., Mottram, C. M., St-Onge, M. R., Möller, C., Strachan, R., Rivers,  
1168 T., and Copley, A.: The metamorphic and magmatic record of collisional  
1169 orogens, *Nature Reviews Earth & Environment*, 2, 781-799,  
1170 10.1038/s43017-021-00218-z, 2021.
- 1171 Winchester, J. A. and Floyd, P. A.: Geochemical discrimination of different  
1172 magma series and their differentiation products using immobile elements,  
1173 *Chemical Geology*, 20, 325-343, [48](https://doi.org/10.1016/0009-</a></p></div><div data-bbox=)





- 1174 2541(77)90057-2, 1977.
- 1175 Wu, C., Yin, A., Zuza, A. V., Zhang, J., Liu, W., and Ding, L.: Pre-Cenozoic  
1176 geologic history of the central and northern Tibetan Plateau and the role of  
1177 Wilson cycles in constructing the Tethyan orogenic system, *Lithosphere*, 8,  
1178 254-292, 10.1130/l494.1, 2016.
- 1179 Wu, F. Y., Wan, B., Zhao, L., Xiao, W. J., and Zhu, R. X.: Tethyan geodynamics,  
1180 *Acta Petrologica Siniaca*, 36, 1627-1674, 2020.
- 1181 Wu, H., Cheng, X., Chen, H., Chen, C., Dilek, Y., Shi, J., Zeng, C., Li, C., Zhang,  
1182 W., Zhang, Y., Lin, X., and Zhang, F.: Tectonic Switch From Triassic  
1183 Contraction to Jurassic-Cretaceous Extension in the Western Tarim Basin,  
1184 Northwest China: New Insights Into the Evolution of the Paleo-Tethyan  
1185 Orogenic Belt, *Frontiers in Earth Science*, 9, 10.3389/feart.2021.636383,  
1186 2021.
- 1187 Xiao, W. J., Windley, B. F., Chen, H. L., Zhang, G. C., and Li, J. L.:  
1188 Carboniferous-Triassic subduction and accretion in the western Kunlun,  
1189 China: Implications for the collisional and accretionary tectonics of the  
1190 northern Tibetan Plateau, *Geology*, 30, 295-298, 10.1130/0091-  
1191 7613(2002)030<0295:Ctsaai>2.0.Co;2, 2002.
- 1192 Xiao, W. J., Windley, B. F., Liu, D. Y., Jian, P., Liu, C. Z., Yuan, C., and Sun, M.:  
1193 Accretionary Tectonics of the Western Kunlun Orogen, China: A Paleozoic–  
1194 Early Mesozoic, Long - Lived Active Continental Margin with Implications  
1195 for the Growth of Southern Eurasia, *The Journal of Geology*, 113, 687-705,  
1196 10.1086/449326, 2005.
- 1197 Xie, F. and Tang, J.: The Late Triassic-Jurassic magmatic belt and its  
1198 implications for the double subduction of the Neo-Tethys Ocean in the



- 1199 southern Lhasa subterrane, Tibet, *Gondwana Research*, 97, 1-21,  
1200 <https://doi.org/10.1016/j.gr.2021.05.007>, 2021.
- 1201 Xie, Y. and Dilek, Y.: Detrital zircon U–Pb geochronology and fluvial basin  
1202 evolution of the Liuqu Conglomerate within the Yarlung Zangbo Suture  
1203 Zone: A critical geochronometer for the collision tectonics of the Tibetan-  
1204 Himalayan Orogenic Belt, *Geosystems and Geoenvironment*, 2, 100178,  
1205 <https://doi.org/10.1016/j.geogeo.2023.100178>, 2023.
- 1206 Xu, W., Zhao, Z., and Dai, L.: Post-collisional mafic magmatism: Record of  
1207 lithospheric mantle evolution in continental orogenic belt, *Science China  
1208 Earth Sciences*, 63, 2029-2041, [10.1007/s11430-019-9611-9](https://doi.org/10.1007/s11430-019-9611-9), 2020.
- 1209 Yan, J.: The early Paleozoic tectono-sedimentary characteristics and the basin-  
1210 orogen process in south Tarim Basin, School of Earth Sciences, Zhejiang  
1211 University, Hangzhou, Zhejiang, China, 137 pp.,  
1212 [10.27461/d.cnki.gzjdx.2022.002783](https://doi.org/10.27461/d.cnki.gzjdx.2022.002783), 2022 (in Chinese with English  
1213 abstract).
- 1214 Yang, Y.-T., Guo, Z.-X., and Luo, Y.-J.: Middle-Late Jurassic  
1215 tectonostratigraphic evolution of Central Asia, implications for the collision  
1216 of the Karakoram-Lhasa Block with Asia, *Earth-Science Reviews*, 166, 83-  
1217 110, <https://doi.org/10.1016/j.earscirev.2017.01.005>, 2017.
- 1218 Zhang, K.-J., Zhang, Y.-X., Tang, X.-C., and Xia, B.: Late Mesozoic tectonic  
1219 evolution and growth of the Tibetan plateau prior to the Indo-Asian collision,  
1220 *Earth-Science Reviews*, 114, 236-249,  
1221 <https://doi.org/10.1016/j.earscirev.2012.06.001>, 2012.
- 1222 Zhang, Q., Wu, Z., Chen, X., Zhou, Q., and Shen, N.: Proto-Tethys oceanic slab  
1223 break-off: Insights from early Paleozoic magmatic diversity in the West



- 1224 Kunlun Orogen, NW Tibetan Plateau, *Lithos*, 346-347, 105147,  
1225 <https://doi.org/10.1016/j.lithos.2019.07.014>, 2019a.
- 1226 Zhang, S., Hu, X., and Garzanti, E.: Paleocene initial indentation and early  
1227 growth of the Pamir as recorded in the western Tarim Basin,  
1228 *Tectonophysics*, 772, 228207, <https://doi.org/10.1016/j.tecto.2019.228207>,  
1229 2019b.
- 1230 Zhang, Z., Xiao, W., Ji, W., Majidifard, M. R., Rezaeian, M., Talebian, M., Xiang,  
1231 D., Chen, L., Wan, B., Ao, S., and Esmaeili, R.: Geochemistry, zircon U-Pb  
1232 and Hf isotope for granitoids, NW Sanandaj-Sirjan zone, Iran: Implications  
1233 for Mesozoic-Cenozoic episodic magmatism during Neo-Tethyan  
1234 lithospheric subduction, *Gondwana Research*, 62, 227-245,  
1235 <https://doi.org/10.1016/j.gr.2018.04.002>, 2018.
- 1236 Zhao, D., Chen, H., Yang, S., Shen, X., Zhu, G., Li, J., Zhang, G., and Xiao, W.:  
1237 Structural style of the foreland fold and thrust belt in the Tianshuihai area,  
1238 Western Kunlun, and its tectonic evolution, *Acta Geologica Sinica*, 74, 134-  
1239 141, 2000 (in Chinese with English abstract).
- 1240 Zhao, G., Wang, Y., Huang, B., Dong, Y., Li, S., Zhang, G., and Yu, S.:  
1241 Geological reconstructions of the East Asian blocks: From the breakup of  
1242 Rodinia to the assembly of Pangea, *Earth-Science Reviews*, 186, 262-286,  
1243 <https://doi.org/10.1016/j.earscirev.2018.10.003>, 2018.
- 1244 Zhao, J., Zeng, X., Tian, J., Hu, C., Wang, D., Yan, Z., Wang, K., and Zhao, X.:  
1245 Provenance and paleogeography of the Jurassic Northwestern Qaidam  
1246 Basin (NW China): Evidence from sedimentary records and detrital zircon  
1247 geochronology, *Journal of Asian Earth Sciences*, 190, 104060,  
1248 <https://doi.org/10.1016/j.jseaes.2019.104060>, 2020.



- 1249 Zhao, Z.-F., Dai, L.-Q., and Zheng, Y.-F.: Postcollisional mafic igneous rocks  
1250 record crust-mantle interaction during continental deep subduction,  
1251 *Scientific Reports*, 3, 3413, [10.1038/srep03413](https://doi.org/10.1038/srep03413), 2013.
- 1252 Zheng, Y., Mao, J., Chen, Y., Sun, W., Ni, P., and Yang, X.: Hydrothermal ore  
1253 deposits in collisional orogens, *Science Bulletin*, 64, 205-212,  
1254 <https://doi.org/10.1016/j.scib.2019.01.007>, 2019.
- 1255 Zhou, C.-A., Song, S., Allen, M. B., Wang, C., Su, L., and Wang, M.: Post-  
1256 collisional mafic magmatism: Insights into orogenic collapse and mantle  
1257 modification from North Qaidam collisional belt, NW China, *Lithos*, 398-  
1258 399, 106311, <https://doi.org/10.1016/j.lithos.2021.106311>, 2021.
- 1259 Zhou, N., Chen, B., Deng, Z., Sang, M., and Bai, Q.: Discovery and Significance  
1260 of Early Jurassic Bimodal Volcanic Rocks in Huoshaoyun, Karakoram,  
1261 *Geoscience*, 33, 990-1002, [10.19657/j.geoscience.1000-8527.2019.05.06](https://doi.org/10.19657/j.geoscience.1000-8527.2019.05.06),  
1262 2019 (in Chinese with English abstract).
- 1263 Zhu, D.-C., Wang, Q., Cawood, P. A., Zhao, Z.-D., and Mo, X.-X.: Raising the  
1264 Gangdese Mountains in southern Tibet, *Journal of Geophysical Research:*  
1265 *Solid Earth*, 122, 214-223, <https://doi.org/10.1002/2016JB013508>, 2017.
- 1266 Zhu, R., Zhao, P., and Zhao, L.: Tectonic evolution and geodynamics of the  
1267 Neo-Tethys Ocean, *Science China Earth Sciences*, 65, 1-24,  
1268 [10.1007/s11430-021-9845-7](https://doi.org/10.1007/s11430-021-9845-7), 2022.
- 1269 Zuza, A. V. and Yin, A.: Balkatach hypothesis: A new model for the evolution of  
1270 the Pacific, Tethyan, and Paleo-Asian oceanic domains, *Geosphere*, 13,  
1271 1664-1712, [10.1130/ges01463.1](https://doi.org/10.1130/ges01463.1), 2017.
- 1272



1273 **Supplementary Materials**

1274 Table S1: Analytical methodology.

1275 Table S2: Zircon U-Pb data of Jurassic basalt and sedimentary rocks.

1276 Table S3: Trace element of zircons.

1277 Table S4: Jurassic conglomerate clast lithologies.

1278 Table S5: Whole rock geochemical results of Jurassic basalts.

1279 Fig. S1: Correlations between the trace elements of Jurassic basalts.

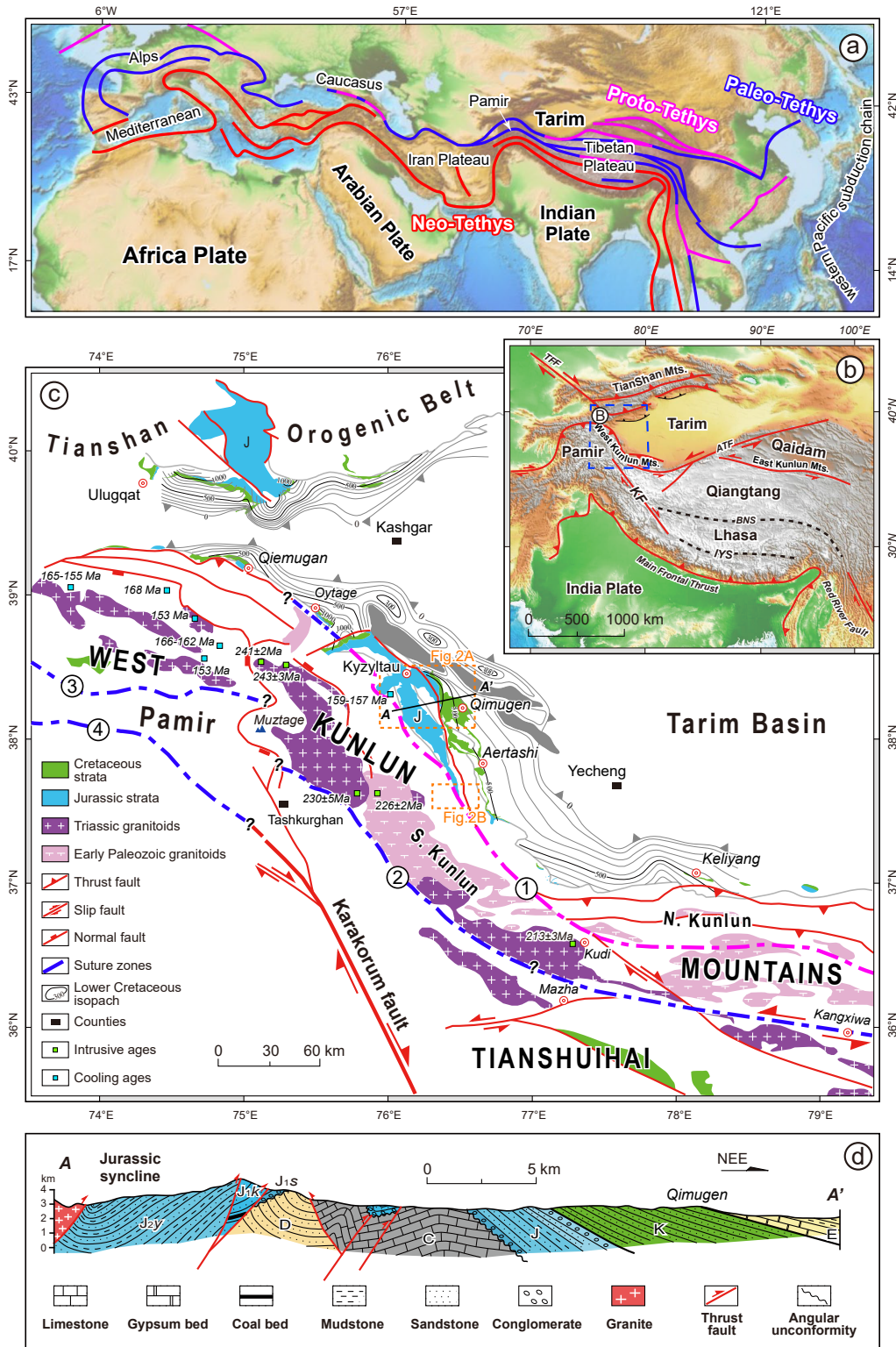




Figure 1 (a) Tectonic plate framework in the Northern Hemisphere and the suture zones within the Tethyan Realm (modified from Wu et al., 2020); (b) Structural framework of central Asia showing main blocks and orogenic belts, with locations of major sutures and boundary faults: TFF-Talas-Fergana Fault, BNS-Bangong-Nujiang suture, IYS-Indus-Yalu suture, ATF-Altyn-Tage Fault; (c) Simplified geologic map of the Western Kunlun Mountains including major units and suture zones (modified from Wu et al., 2021; cooling ages of basements refer to Yang et al., 2017): ①- Early Paleozoic Kudi suture, ②- Triassic Mazar-Kangxiwa suture, ③- Triassic Tanyamas suture separating the North and Central Pamirs, ④- Rushan-Pshart zone separating the Central and South Pamirs; (d) A section across the east part of the Western Kunlun Mountains showing the deformed and fragmented Jurassic basin. The section location is presented in Fig.1 (b).

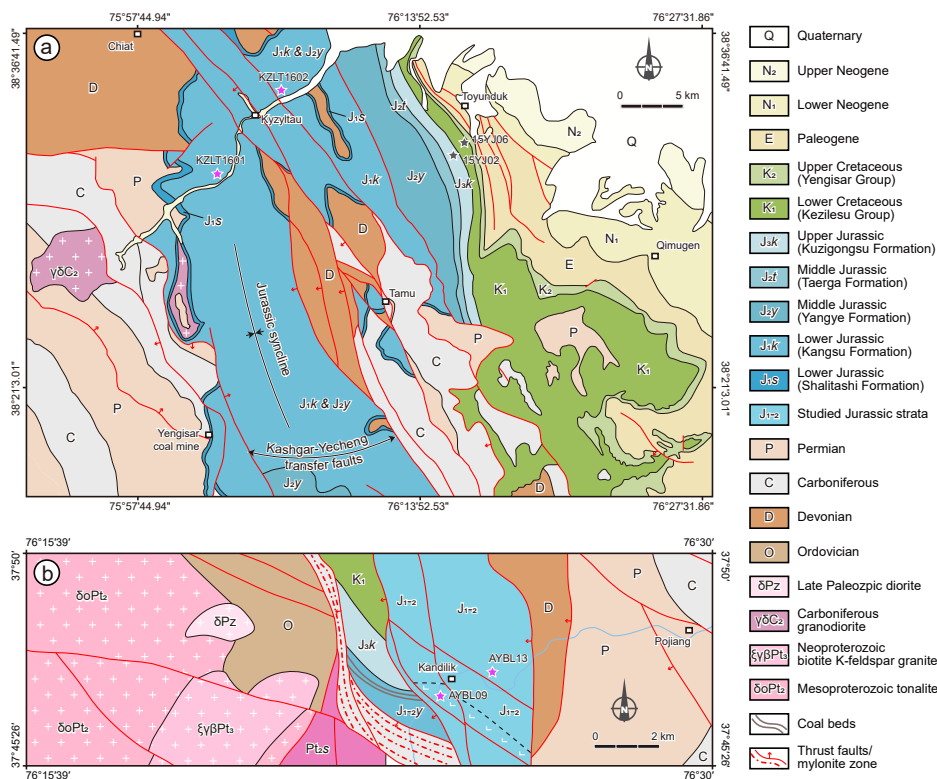


Figure 2 (a) Geological map in the Kyzyltau region showing the stratigraphic information and sampling locations ; (b) Geological map in the Kandilik region showing the Proterozoic basements and Paleozoic-Mesozoic strata. The red stars mark sampling locations in this work, and the grey stars mark the locations of published data (Zhang et al., 2019b).



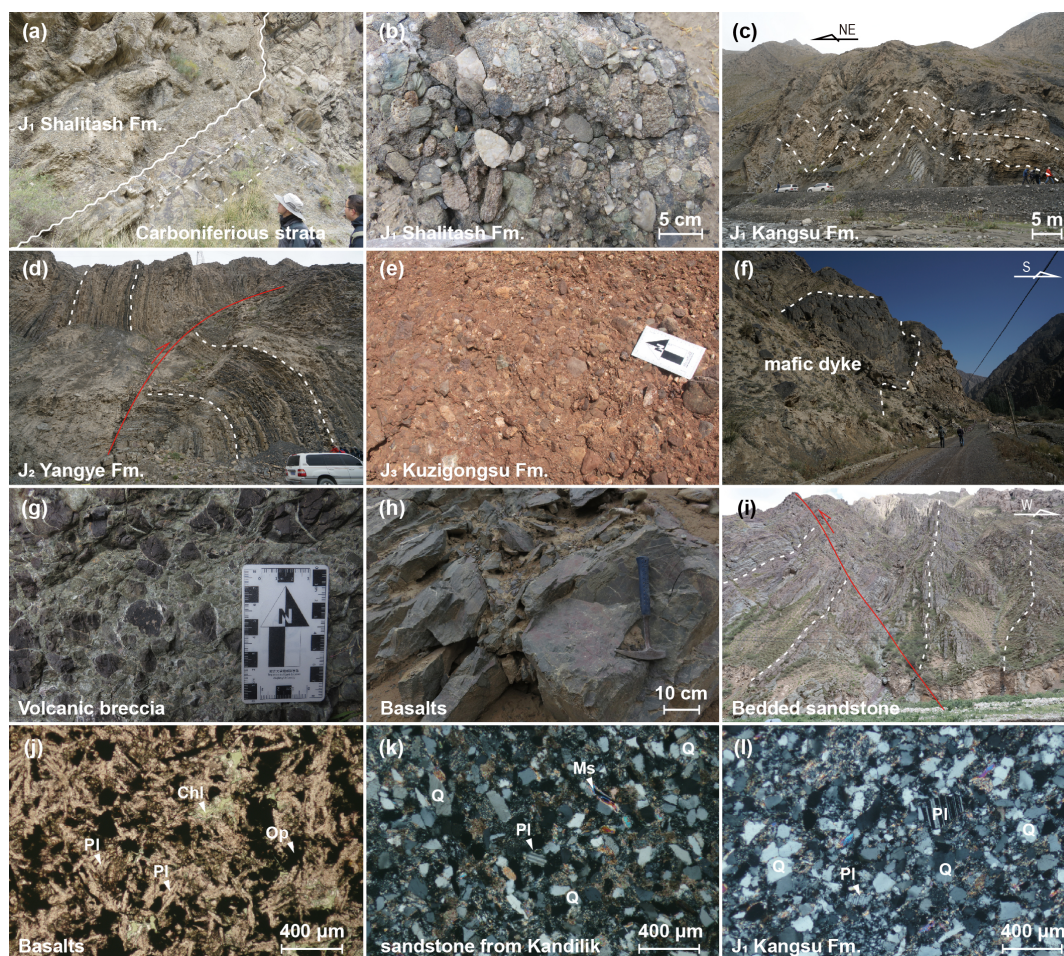


Figure 3 Photographs showing the observation from field and binocular microscope. (a) Early Jurassic Shalitash Formation overlying on the deformed Carboniferous strata with angular unconformity; (b) Conglomerate clast lithologies in the Shalitash Formation; (c) Early Jurassic Kangsu Formation with strongly deformed sandstone layers; (d) Strong deformation of the turbidite sequences in the Middle Jurassic Yangye Formation; (e) Conglomerate clast lithologies in the Late Jurassic Kuzigongsu Formation; (f) Mafic dyke within newly identified Jurassic strata in the Kandilik region; (g) Basaltic volcanic breccia; (h) Massive basalt layer; (i) Jurassic bedded feldspar lithic sandstones with great thickness, which was previously assigned to be Precambrian age; (j) Micrograph of basalt under plane-polarized light; (k) Micrograph of Jurassic sandstone under cross-polarized light from Kandilik section; (l) Micrograph of Jurassic sandstone under cross-polarized light from Kyzyltau section.

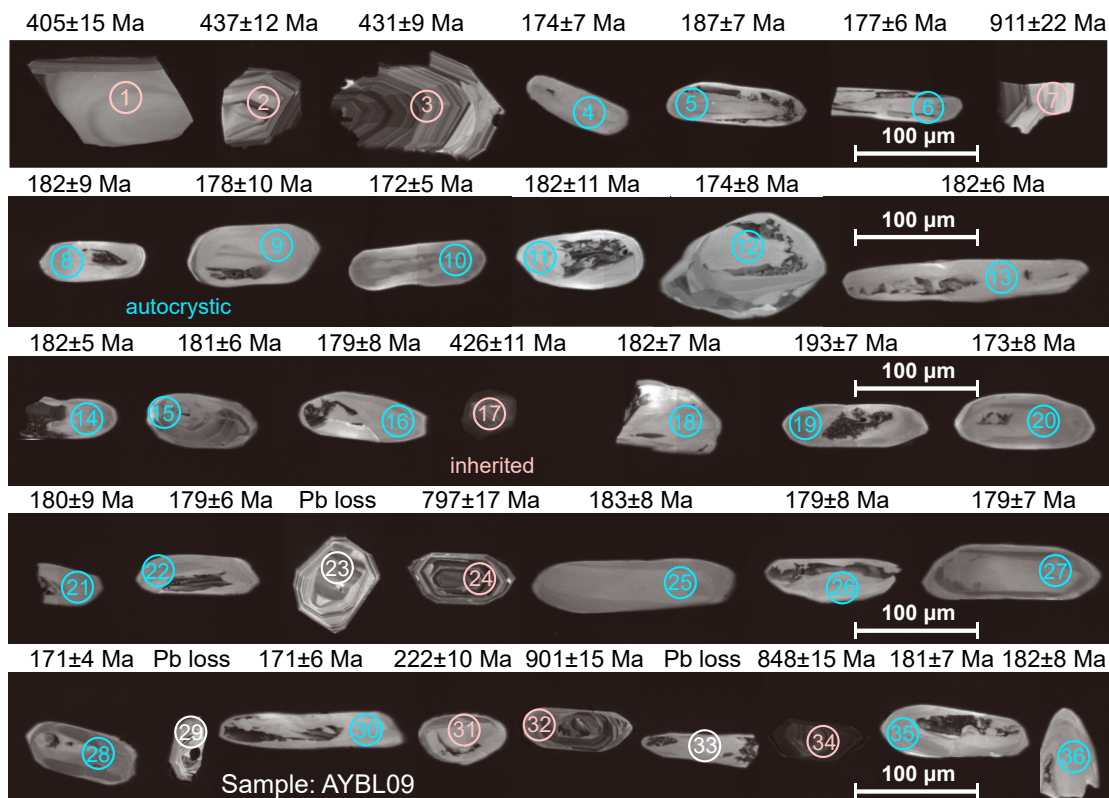


Figure 4 CL images of various kinds of zircons in basalt sample AYBL09, noting the apparent  $^{206}\text{Pb}/^{238}\text{U}$  ages above.

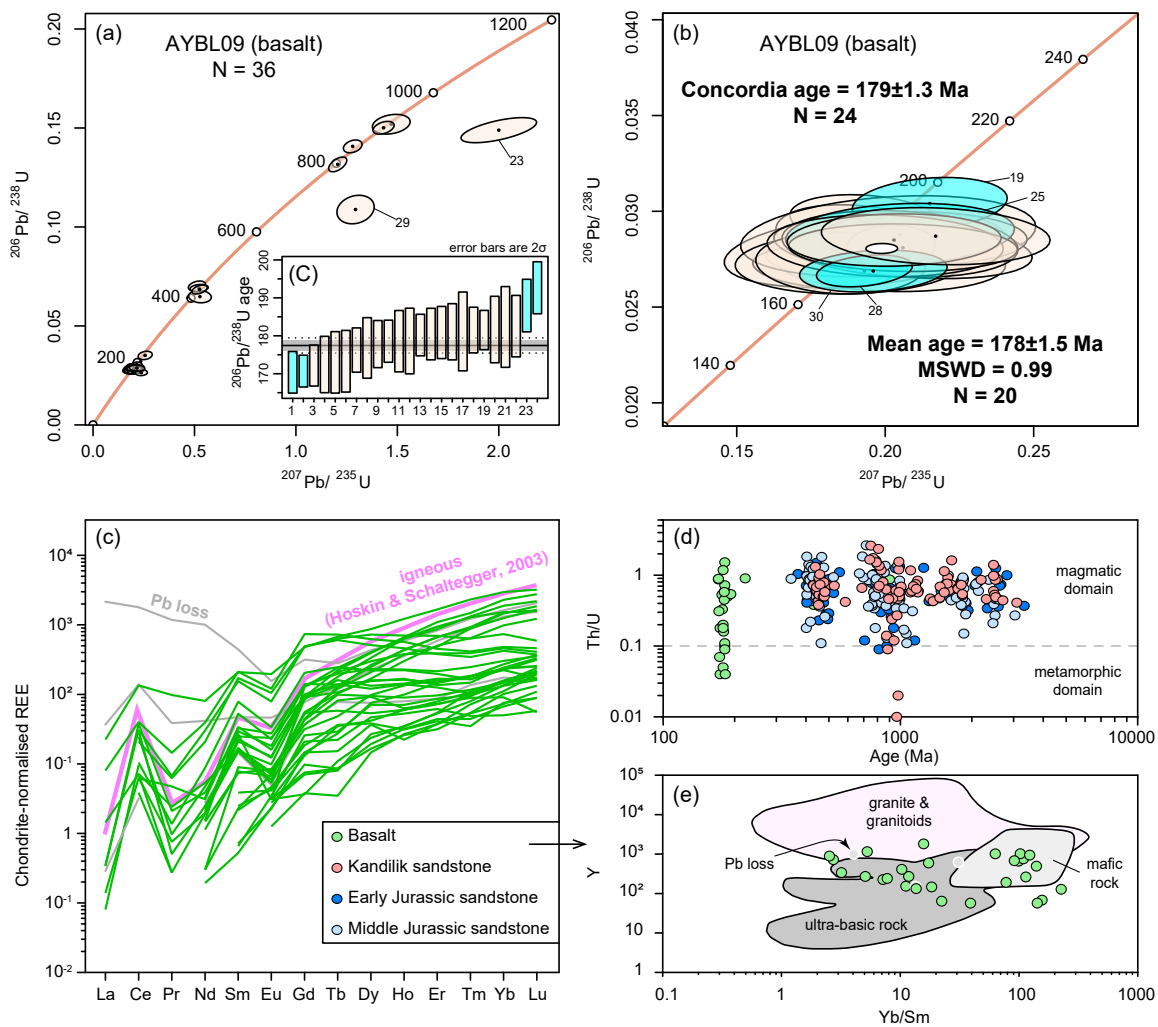


Figure 5 (a) Concordia plot of LA-ICP-MS U-Pb analysis for the zircons of the basalt sample AYBL09; (b) Weighted mean  $^{206}\text{Pb}/^{238}\text{U}$  age and concordia age of the youngest zircon groups; (c) Zircon chondrite-normalised REE pattern of the basalt; (d) Th/U ratios of zircons from basalt and sandstone samples. (e) Yb/Sm-Y plotting to distinguish the origins of zircons from the basalt.

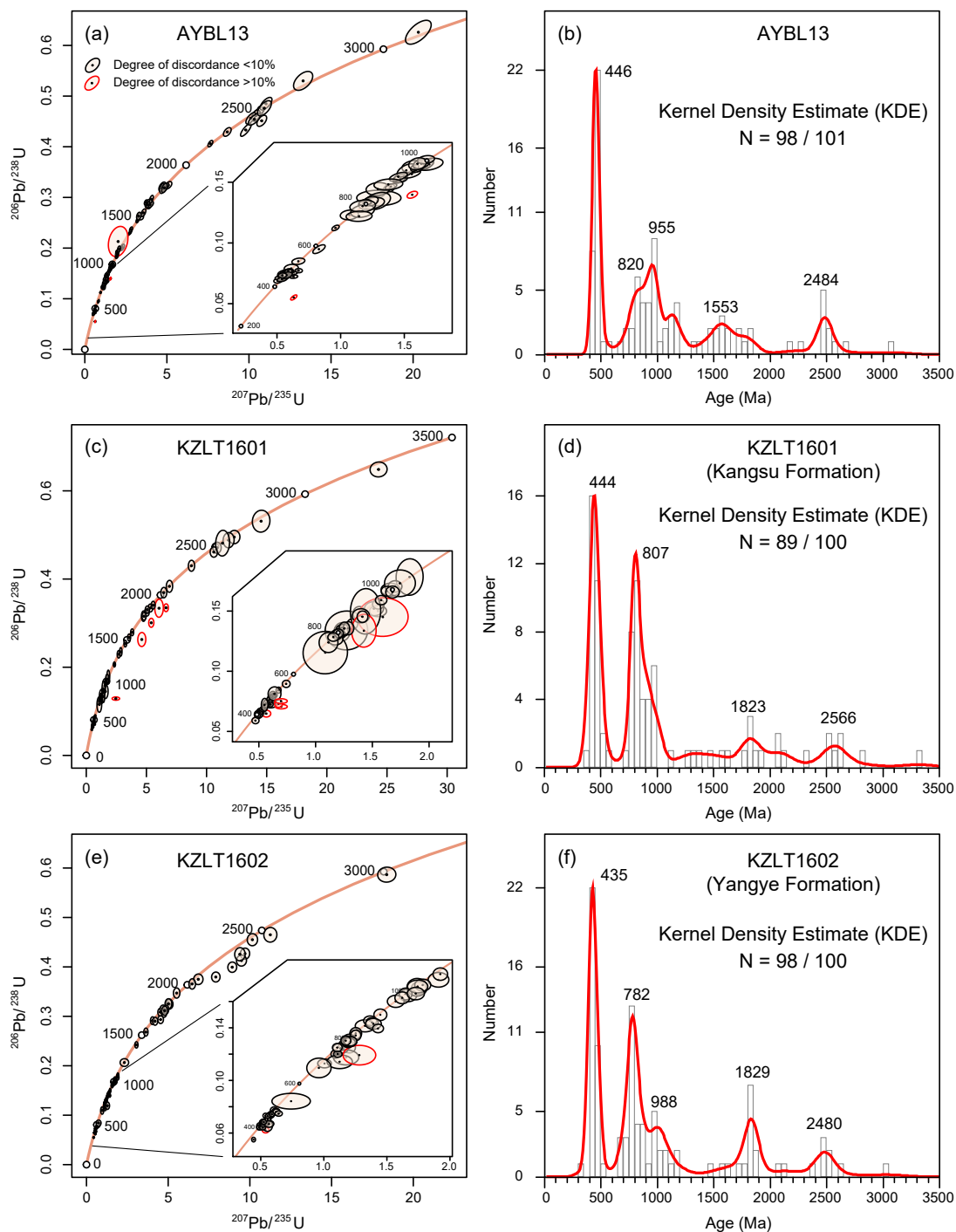


Figure 6 Concordia diagram for the detrital zircons of (a) sample AYBL13 from Kandilik section, (c) sample KZLT1601 from Kangsu Formation, and (e) sample KZLT1602 from Yangye Formation; Diagram of the Kernel Density Estimate of detrital zircon U-Pb ages for (b) AYBL13, (d) KZLT1601, and (f) KZLT1602.

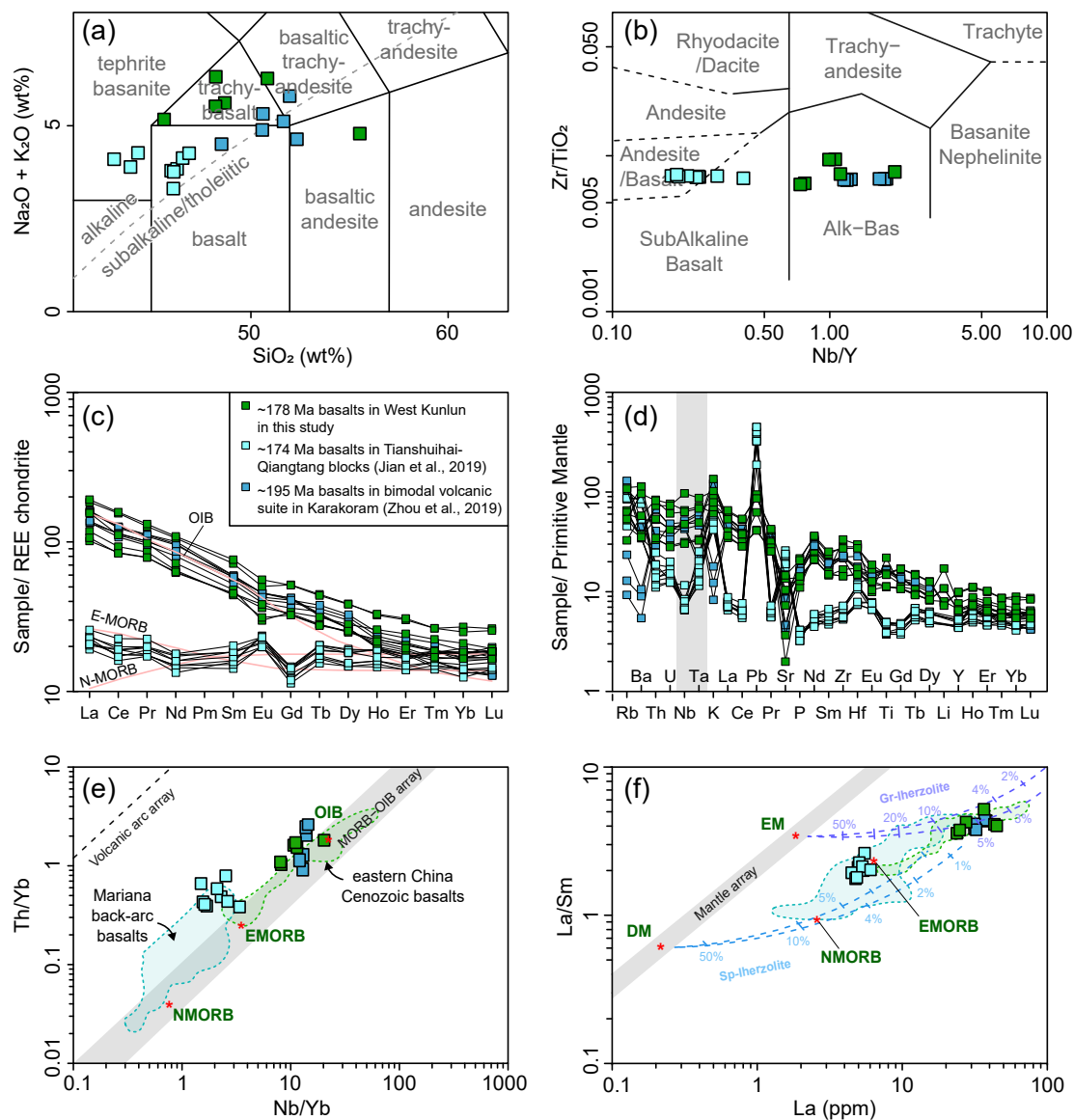


Figure 7 Geochemical classification diagram of Jurassic basalt samples from the Kandilik region in the West Kunlun Mountains (green) and from Longshan Formation in the Tianshuihai terrane (blue): (a) total alkali versus silica (Middlemost, 1994) and (b) Zr/TiO<sub>2</sub> vs. Nb/Y diagrams (Winchester and Floyd, 1977); (c) Rare earth elements pattern (REE) and (d) trace element diagrams of Jurassic basalts; (e) Th/Yb vs. Nb/Yb plot (Pearce, 2008) and (f) La/Sm vs. La plot (Aldanmaz et al., 2000) Chondrite-normalized REE and the primitive mantle-normalized values refer to Sun and McDonough (1989). The range of the Mariana back-arc basalts refers to Pearce (2008) and the range of eastern China Cenozoic basalts refers to Guo et al. (2020).

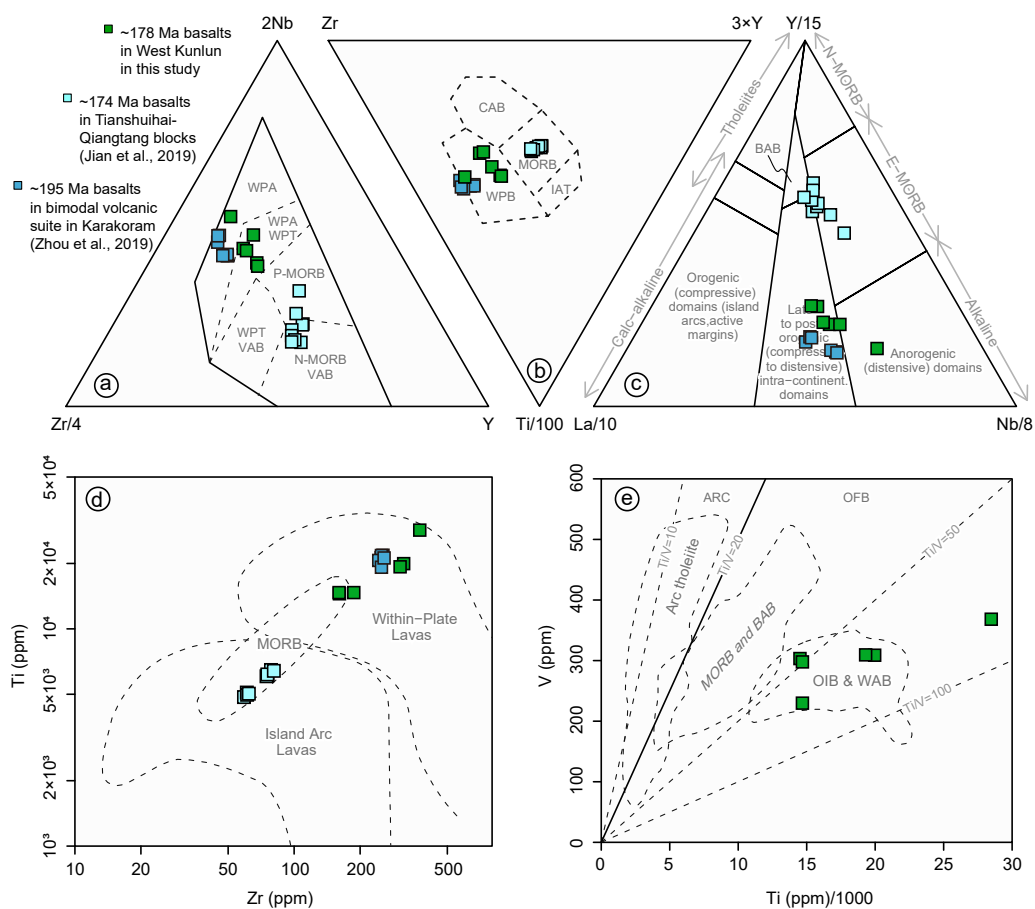
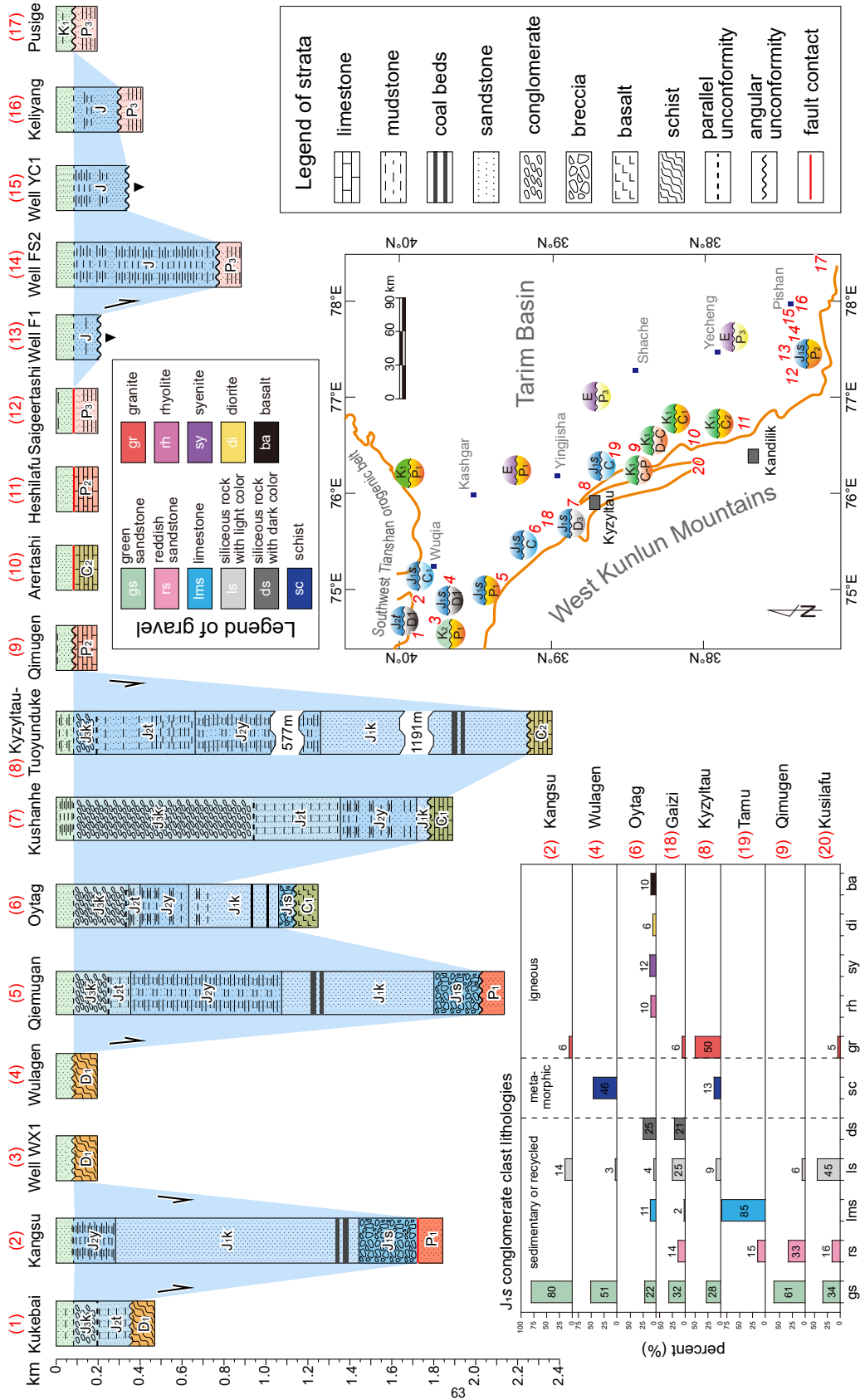


Figure 8 Tectonic discrimination diagrams for Jurassic basalts through (a) Zr/4-2Nb-Y plot and (b) Zr-3Y-Ti/100 plot (Meschede, 1986), (c) La/10-Y/15-Nb/8 plot (Cabanis and Lecolle, 1989), (d) Ti-Zr plot (Pearce, 1982) and (e) V-Ti/1000 plot (Rollinson, 1993). Abbreviation: WPB-within plate basalts; WPA- within plate alkali basalts; WPT-within plate tholeiites; VAB-volcanic arc basalts; CAB- calc-alkali basalts; IAT-island arc tholeiites; BAB-back arc basalts.



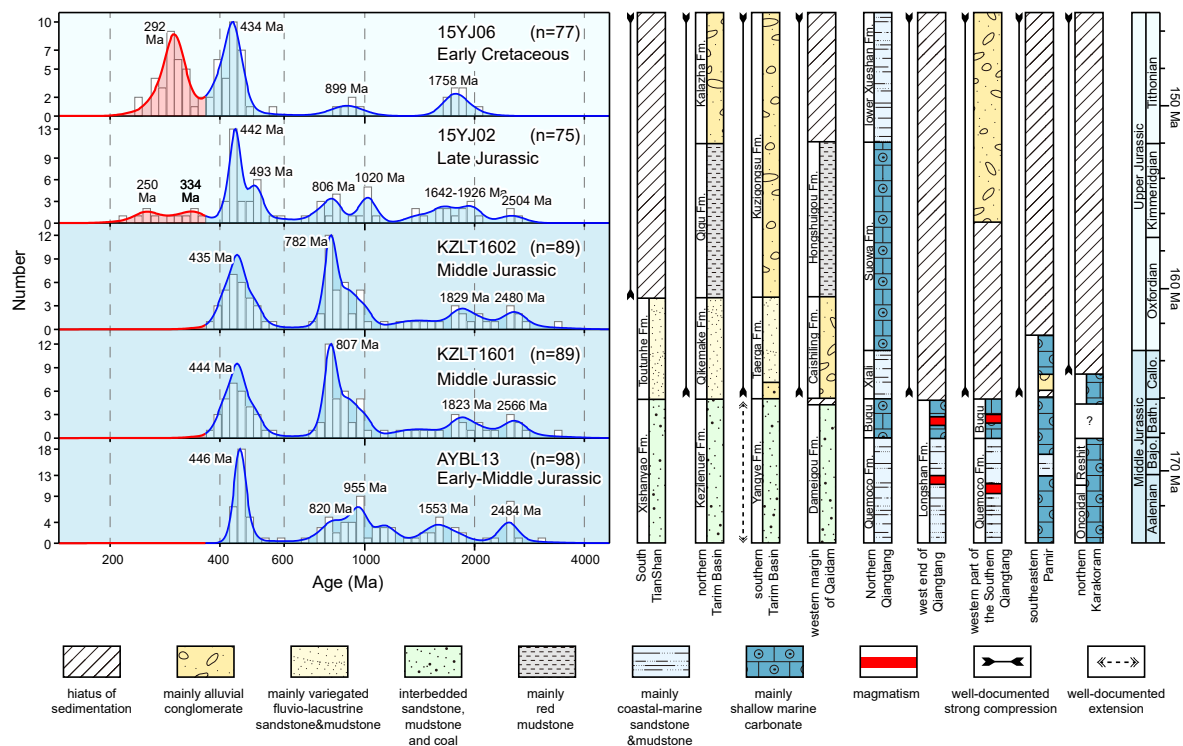


Figure 10 Late Jurassic basin inversion based on the provenance variation through the Early Jurassic to Early Cretaceous and the stratigraphic correlation in the northwestern China. Late Jurassic and Early Cretaceous sandstone samples are according to Zhang et al. (2019b), stratigraphic correlation is modified from Yang et al. (2017).



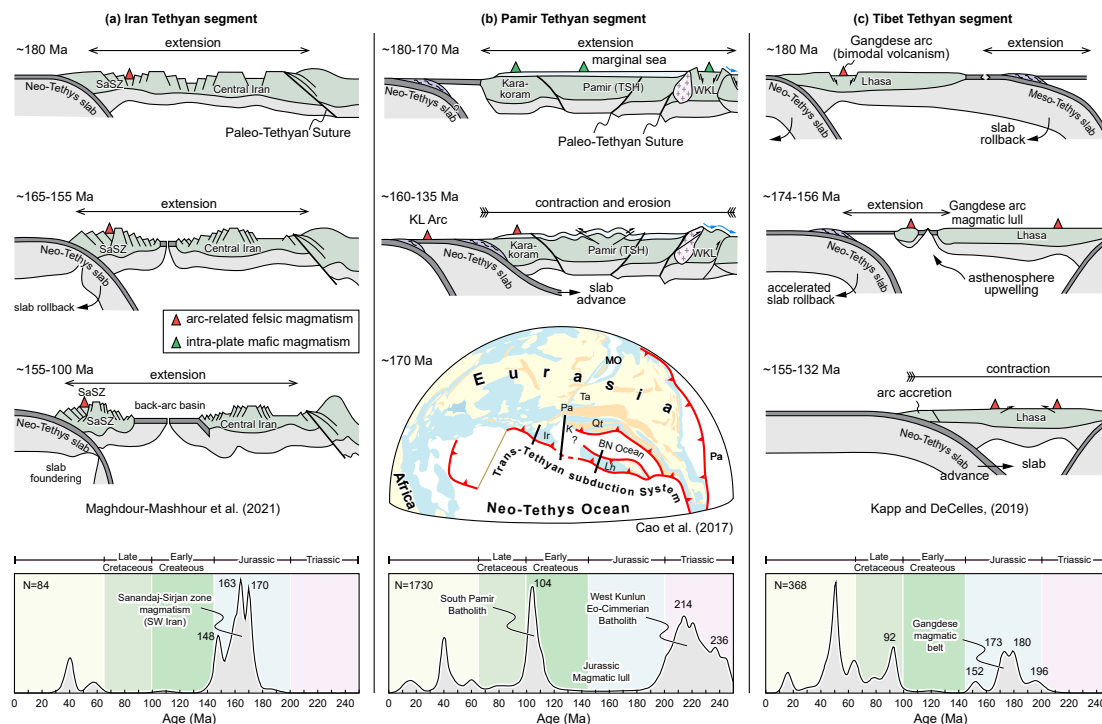


Figure 11 Illustrative cartoons indicating the tectonic variation of the southern Eurasian margin in Jurassic. The subduction of the Neo-Tethys Ocean resulted in persistent rifting along the Iran Tethyan segment, generating massive magmatism during the Early Jurassic to Early Cretaceous. The far-field subduction causing the Early-Middle Jurassic extension along the Pamir Tethyan segment without magmatic flare-up. The changes in subduction style along the Pamir and Tibet Tethyan segments induced the extension-contraction transition. The spatial magmatic datasets are according to Zhang et al. (2018), Chapman et al. (2018), Ma et al. (2017) and Zhu et al. (2017), and the map of paleogeographic reconstruction is modified from Cao et al. (2017). Abbreviation: SaSZ-Sanandaj-Sirjan zone; TSH-Tianshuihai block; WKL-West Kunkun Mountains; KL Arc- Kohistan Ladakh Arc; Ir-Iran; K-Karakoram; Pa-Pamir; Ta-Tarim; QT-Qiangtang; Lh-Lhasa; BN Ocean-Bangong-Nujiang Ocean.